

Impact of Dry Intrusion Events on Composition and Mixing State of Particles During Winter ACE-ENA Study

Jay M. Tomlin¹, Kevin A. Jankowski¹, Daniel P. Veghte^{3,4}, Swarup China⁴, Peiwen Wang⁵,
5 Matthew Fraund⁶, Johannes Weis⁶, Guangjie Zheng^{7,8}, Yang Wang^{8,9}, Felipe Rivera-Adorno¹,
Shira Raveh-Rubin¹⁰, Daniel A. Knopf⁵, Jian Wang^{7,8}, Mary K. Gilles⁶, Ryan C. Moffet¹¹,
Alexander Laskin^{1,2*}

¹Department of Chemistry, ²Department of Earth Atmospheric and Planetary Sciences, Purdue University, West Lafayette, IN 47907, USA

10 ³Center for Electron Microscopy and Analysis, Ohio State University, Columbus, OH 43212, USA

⁴Environmental Molecular Sciences Laboratory, Pacific Northwest National Laboratory, Richland, WA 99354, USA

⁵School of Marine and Atmospheric Sciences, Stony Brook University, Stony Brook, NY 11794, USA

⁶Chemical Sciences Division, Lawrence Berkeley National Laboratory, Berkeley, CA 94720, USA

15 ⁷Center for Aerosol Science and Engineering, Department of Energy, Environmental and Chemical Engineering, Washington University in St. Louis, St. Louis, MO 63130, USA

⁸Environmental and Climate Science Department, Brookhaven National Laboratory, Upton, NY 11973, USA

⁹Department of Civil, Architectural and Environmental Engineering, Missouri University of Science and Technology, Rolla, MO 65409, USA

¹⁰Department of Earth and Planetary Sciences, Weizmann Institute of Science, Rehovot 76100, Israel

20 ¹¹Sonoma Technology, Inc., Petaluma, CA 94954, USA

Correspondence to: Alexander Laskin (alaskin@purdue.edu)

Abstract. Long-range transport of continental emission has far reaching influence over remote regions resulting in substantial change in the size, morphology, and composition of the local aerosol population and cloud condensation nuclei (CCN) budget. Here, we investigate the physicochemical properties of atmospheric particles collected onboard a research aircraft flown over the Azores during the winter 2018 Aerosol and Cloud Experiment in the Eastern North Atlantic (ACE-ENA) campaign. Particles were collected within the marine boundary layer (MBL) and free troposphere (FT), after long-range atmospheric transport episodes facilitated by dry intrusion (DI) events. Chemical and physical properties of individual particles were investigated using complementary capabilities of computer-controlled scanning electron microscopy and X-ray spectro-microscopy to probe particle external and internal mixing state characteristics. Furthermore, real-time measurements of aerosol size distribution, cloud condensation nuclei (CCN) concentration, and back trajectory calculations were utilized to help bring into context the findings from off-line spectromicroscopy analysis. While carbonaceous particles were found to be the dominant particle-type in the region, changes in the percent contribution of organics across the particle population (i.e., external mixing) shifted from 68% to 43% in the MBL and from 92% to 46% in FT samples during DI events. This change in carbonaceous contribution is counterbalanced by the increase of inorganics from 32% to 57% in the MBL and 8% to 55% in FT. The quantification of organic volume fraction (OVF) of individual particles derived from X-ray spectro-microscopy, which relates to the multi-component internal composition of individual particles, showed a factor of 2.06 ± 0.16 and 1.11 ± 0.04 increase in the MBL and FT, respectively, among DI samples. We show that supplying particle OVF into the κ -Köhler equation can be used as a good approximation of field measured in-situ CCN concentrations. We also report changes in the κ values between $\kappa_{\text{MBL, non-DI}} = 0.48$ to $\kappa_{\text{MBL, DI}} = 0.41$ and $\kappa_{\text{FT, non-DI}} = 0.36$ to $\kappa_{\text{FT, DI}} = 0.33$, which is consistent with enhancements in OVF followed by the DI episodes. Our observations suggest that entrainment of particles from long-range continental sources alters the mixing state population and CCN properties of aerosol in the region. The work presented here provides field observation data that can inform atmospheric models that simulate sources and particle composition in the Eastern North Atlantic.

1 Introduction

45 Marine low clouds play significant role in the world's climate and energy balance (Wood et al., 2015). They are the major factor
in increasing the Earth's albedo – fraction of solar energy reflected back into space leading to an overall cooling effect (Wood,
2012; Wood et al., 2015). Marine low clouds represent one of the leading sources of uncertainty in atmospheric models due to
50 limited observational data, insufficient understanding of the microphysical changes that regulate these clouds, and the lack in fine
model resolution to account for such processes (Bony, 2005; Klein et al., 2013). Other relevant boundary layer processes also
contribute to the challenges in assessing marine low clouds such as turbulent mixing, entrainment, and emissions of aerosols and
their precursors (Pincus and Baker, 1994; Ackerman et al., 2004). In particular, the response of low altitude clouds is sensitive to
aerosol perturbations, which requires a greater understanding on the processes that govern regional aerosol budget and source
attribution (Levin and Cotton, 2009; Altaratz et al., 2014; Rosenfeld et al., 2019; Zheng et al., 2018, 2021). Source dependent
particle size and composition can lead to changes in the clouds albedo and precipitation due to their varying efficiency to act as
55 cloud condensation nuclei (CCN) and ice nucleating particles (INP) (Johnson et al., 2004; Hamilton et al., 2014; Zheng et al.,
2020a).

Atmospheric particles exhibit complex internal heterogeneity (Murphy and Thomson, 1997; Buseck and Posfai, 1999; Prather et
al., 2008; Li et al., 2016; Riemer et al., 2019; Laskin et al., 2019). These particles can come from direct emissions (i.e., primary
particles), or from gas-particle conversion in atmospheric reactions (i.e., secondary particles) (Reddington et al., 2011). Primary
60 particles with complex composition include primary organic aerosols, elemental carbon (i.e., black carbon/soot), inorganic species
from combustion and biomass burning sources (Toner et al., 2006; Souri et al., 2017), and sea spray aerosol with organic
components influenced by ocean biological activity (Prather et al., 2013; Pham et al., 2017). On the other hand, secondary organic
aerosol (SOA) is formed from the oxidation products of volatile organic compounds (VOCs) of either biogenic or anthropogenic
origin. Secondary fine particles of nitrate and sulfate are similarly formed from the oxidation of their inorganic gaseous precursors
65 NO_x and SO₂, respectively (National Research Council (U.S.), 2002). In marine areas, formation of sulfate aerosol is further
influenced by gas-phase emissions of dimethyl sulfide (DMS) from biota, which upon oxidation yield low volatility products such
as sulfuric acid (H₂SO₄) (Kulmala et al., 2000) and methylsulfonic acid (MSA) (Andreae et al., 1985; Hodshire et al., 2019).
Physical and chemical characteristics of individual particles such as morphology, chemical composition, hygroscopicity, lifetime,
and chemical mixing state have a profound effect on their CCN activity (Cruz and Pandis, 1997; VanReken, 2003; King et al.,
70 2012; Schmale et al., 2017; Riemer et al., 2019). Note that the term “chemical mixing state” refers to how various chemical species
are mixed within individual particles (Riemer et al., 2019). The chemical mixing state depends on emission sources and
atmospheric ageing events which include, but are not limited to, biomass burning influence (Levin et al., 2010), anthropogenic
emissions (Jacobson, 2001), large continental dust events (Fraund et al., 2017; Adachi et al., 2020). For example, previous studies
found that within a few hours urban non-hygroscopic aerosol (i.e., mixed organic and black carbon aerosol) can accumulate a
75 sufficient coating of hygroscopic sulfates and nitrates to increase their hygroscopicity parameter (κ) (Petters and Kreidenweis,
2007) from 0 to 0.1 (Wang et al., 2010).

The variability within individual atmospheric particles has been well documented by both model and field measurements across
different regions worldwide such as urban (Wang et al., 2010; Ault et al., 2010, 2012; Wang et al., 2012; Fraund et al., 2017; Ren
et al., 2018), rural (Vakkari et al., 2018; Tomlin et al., 2020), remote forested areas (Bondy et al., 2018), Arctic (Gunsch et al.,
80 2017; Gonçalves et al., 2021), and marine (Ault et al., 2013; Zheng et al., 2020a, b). Long-range transport and meteorological
processes such as dry intrusions (DI) and vertical mixing of air also play a significant role in the continuous evolution of particle
composition in the atmosphere (Raes, 1995; Pratt and Prather, 2010; Cubison et al., 2011; Igel et al., 2017; Zheng et al., 2020b).

DI are events of dry, slantwise descending airflow from the upper troposphere in midlatitudes down through the boundary layer at lower latitudes (Raveh-Rubin, 2017). Such intrusions of dry air, typically peaking in winter, occur with the passage of extratropical cyclones and their trailing cold fronts, i.e., in the post cold-frontal region (Wernli, 1997; Browning, 1997; Catto and Raveh-Rubin, 2019). Events of DI are strongly coupled to the boundary layer, which cools and deepens during DI, and were shown to induce enhanced ocean heat fluxes (Raveh-Rubin and Catto, 2019; Iltoviz et al., 2021). DI events are of particular interests as they can contain air mass with a complex distribution of aged particles having drastically different size, morphology, and composition compared to local regional aerosols, leading to changes in the local aerosol-cloud interactions and cloud lifetimes (Zheng et al., 2020b; Wang et al., 2020). For example, it has been shown that the CCN population in the remote marine boundary layer (MBL) of Eastern North Atlantic can be influenced by long-range transport of wildfire aerosols originating from North America (Zheng et al., 2020b; Wang et al., 2021b). The properties of these wildfire aerosols facilitated by long-range transport processes alters as it undergoes ageing (e.g. multiphase particle chemistry, photo-bleaching and gas-particle partitioning of organics), resulting in changes in both the optical properties and the cloud-forming potential (Jacobson, 2001; Levin et al., 2010; Zheng et al., 2020b). In particular, aged wildfire aerosol is typically dominated by accumulation mode particles, which readily serve as CCN in the region despite a substantially lower κ value (i.e., 0.2 to 0.4) than regional highly hygroscopic aerosol of marine origin (e.g. sea spray aerosol, $\kappa = 1.1$) (Zieger et al., 2017; Zheng et al., 2020b). Lastly, long-range transported and atmospherically aged free tropospheric particles can contribute to the ice-nucleating particle population and potentially impact cloud formation (China et al., 2017).

This paper investigates the physicochemical properties of atmospheric particles during the Aerosol and Cloud Experiment in the Eastern North Atlantic (ACE-ENA) field campaign conducted at the Azores in January-February 2018. Aircraft measurements and onboard sampling of particles (followed by laboratory-based particle analysis) were utilized to characterize the difference in the contributions of various sources to FT and MBL aerosols under representative synoptic conditions (i.e., DI vs. non-DI periods) in this geographical area. Particle analysis included particle-type classification with statistical depth provided by computer-controlled scanning electron microscopy and a subset of particles were sampled by X-ray spectro-microscopy to characterize particle chemical mixing state (internal heterogeneity). The particle-type composition, chemical mixing state, and morphology from analyzed periods were then combined with real-time measurement of aerosol size distribution, CCN concentration, and back trajectory calculations to obtain the representative composition of particles present in the MBL during the DI events and entrainment of particles originated from North America. The data presented here provides observational input for atmospheric process models to simulate sources and particle composition in the broader North Atlantic region.

2 Experimental Methods

2.1 Field Campaign and Meteorological Conditions

Samples of atmospheric particles were collected aboard the U.S. Department of Energy Gulfstream aircraft (G-1). Flight patterns were flown between Terceira Island (38° 45' 43" N, 27° 5' 27" W) and Graciosa Island (39° 3' 12" N, 28° 7' 26" W), Portugal and within 20–30 km of Graciosa Island (Wang et al., 2021a). Flight plans were based on the projected meteorological conditions from various global forecast modes including Monitoring Atmospheric Composition and Climate, Global Forecast System, and European Centre for Medium-Range Weather Forecasts (ECMWF). A subset of collected samples was selected for analysis based on synoptic conditions (identifying DI vs. non-DI periods) and altitudes (clear MBL and FT layers) for each day. Samples analyzed were collected during the second Intensive Operation Period of ACE-ENA, on the dates of 2018-01-19, 2018-01-21, 2018-01-24, 2018-01-25, 2018-01-26, 2018-01-28, 2018-01-30, 2018-02-01, 2018-02-08, 2018-02-11, 2018-02-15, 2018-02-16, 2018-02-19.

These dates were selected due to unique transport episodes that associated with the sampling periods. DI days we identified objectively using the Lagrangian analysis tool (LAGRANTO) version 2.0 (Sprenger and Wernli, 2015) and wind field data obtained from the ECMWF interim reanalysis (ERA-Interim) with available 6-hourly, interpolated to $1^{\circ} \times 1^{\circ}$ horizontal grid resolution, at 60 vertical hybrid levels (Dee et al., 2011). DI were identified by a systematic calculation of forward trajectories at altitudes higher than 600 hPa, while the DI trajectories were identified based on the vertical descent of the airmasses. For a trajectory to be termed a DI, their pressure must increase (i.e., descend in altitude) by at least 400 hPa in 48 hrs (Raveh-Rubin, 2017). If such a DI trajectory is found within a 3-degree radius circle around Graciosa, the date is considered as 'DI'. In addition, backward trajectories for each sampling period were calculated for the end points at relevant flight altitudes (Figure S1 and S2) using the Hybrid Single-Particle Lagrangian Integrated Trajectory (HYSPPLIT) model (Stein et al., 2015; Rolph et al., 2017). Atmospheric data from ERA Interim are analyzed additionally for the atmospheric column at Graciosa, namely, potential temperature, equivalent potential temperature, potential vorticity and boundary-layer height. The latter is diagnosed in ERA Interim using the critical bulk Richardson number, upon its first passing of the threshold 0.25, when scanning from the surface upwards (ECMWF, 2007).

2.2 Particle Collection and In-Situ Measurements of Particle and Cloud Properties

The G-1 aircraft is equipped with sensor modules to deliver precise real-time inertial measurement, GPS, meteorological, and turbulence data such as position, altitude, temperature, pressure relative humidity, and three-dimensional winds. For particle collection, the G-1 was equipped with an isokinetic aerosol inlet, from which ambient aerosol was transported to individual instruments. Particle samples were collected using a custom built time-resolved aerosol collector (TRAC) that autonomously collected particles on substrates at preset time intervals (Laskin et al., 2006). The TRAC is a single stage impactor with an aerodynamic cutoff size ($D_{50\%}$) of $0.36 \mu\text{m}$ (Laskin et al., 2003) coupled to a rotating disk that can hold up to 160 samples. The disk was preloaded with microscopy substrates (Carbon Type-B film coated 400 mesh copper grids, Ted Pella, Inc.). The sampling was performed at a single spot on the center of each substrate for 7–10 min, depending upon the flight. After each flight, sample discs were taken off the TRAC, plated, and hermetically sealed prior to transport. Once samples were received in the lab, the sample grids used for the analysis were removed from the sealed plate and transferred into TEM grid boxes stored at room temperature and dry conditions in a desiccator cabinet. Online measurements of aerosols aboard the G-1 include a passive cavity aerosol spectrometer-100X probe (PCASP, $D_p = 0.1\text{--}3.0 \mu\text{m}$, 1 Hz resolution) and a fast integrated mobility spectrometer (FIMS, $D_p = 0.01\text{--}0.5 \mu\text{m}$, 1 Hz resolution), which provided size distributions and concentrations of ambient particles (Kulkarni and Wang, 2006; Wang et al., 2018). During all research flights, a Nafion dryer reduced the relative humidity of the air stream in the sampling line. A CCN counter (Droplet Measurement Technologies) measured the concentration of particles that activate at a supersaturation of 0.14%. A high-resolution time-of-flight aerosol mass spectrometer (HR-ToF-AMS) was deployed onboard to characterize bulk non-refractory aerosol composition (i.e., organics, sulfate, ammonium, and chlorine) (DeCarlo et al., 2006; Zawadowicz et al., 2021). The particle size distributions and CCN concentrations were analyzed when the liquid water content was below 0.001 g/m^3 to avoid periods when cloud shattering artifacts could influence the sampled particles (Korolev et al., 2011). The liquid water content was obtained by integrating the droplet size distributions measured by a fast cloud droplet probe (FCDP; Droplet Measurement Technologies).

Additional information on the sampling conditions is presented in the Table S1 of the supplemental file and includes sampling time/date, average sampling altitude, boundary layer height, particle concentration, and wind speed. The boundary layer height was calculated based on potential temperature measurements collected for each flight. The boundary layer is limited by a well-defined temperature inversion resulting in a maximum value of the temperature gradient as a function of height (Stull, 1988). A

160 summary of each flight (altitude and aerosol particle concentration vs. time) with the collection times highlighted is shown in
Figures S3 and S4. Guided by meteorological analysis and wind field data to identify DI periods, we performed offline microscopy
analysis of collected particle samples across different atmospheric layers and transport episodes during the ACE-ENA campaign.

2.3 Methods of Particle Analysis

Morphology and elemental analysis of individual particles was performed using computer-controlled scanning electron microscopy
165 coupled with energy dispersive X-ray spectroscopy operated at 20 kV (CCSEM/EDX; FEI Quanta 3D, EDAX Genesis). During
CCSEM/EDX analysis particle samples were systematically imaged and particles larger than 100 nm are recognized. Of note, the
particle size reported from CCSEM/EDX analysis is defined as the area equivalent diameter (AED, μm), which is based on fitting
a circle with area equivalent to the particle's 2D projected image. This is followed by an automated acquisition of their individual
EDX spectra for each particle (Laskin et al., 2005). EDX spectra with sufficient X-ray counting statistics (40–1500 photons/s)
170 were then processed to quantify relative atomic fractions of 15 elements: C, N, O, Na, Mg, Al, Si, P, S, Cl, K, Ca, Mn, Fe, and Cu.
The EDX peak of Cu is heavily influenced by a background signal from the copper TEM grid and the sample holder made of
beryllium-copper alloy. Therefore, quantified atomic fractions of Cu were excluded from particle-type classification of the
analyzed particles. Two independent methods were employed for the particle-type grouping and classification: (1) *k*-means
clustering and (2) rule-based particle classification. The *k*-means clustering is an unsupervised machine learning algorithm
175 designed to group similar data sets without user intervention (Rebotier and Prather, 2007; Moffet et al., 2012). The second approach
for the categorization of particles utilizes a series of user-defined rules to separate analyzed particles into groups of typical
elemental contribution (Laskin et al., 2012). For this work, the *k*-means clustering was used as a primary method for particle-type
classification while the rule-based approach was used as a complementary method to build confidence on the identification of
different particle-types. Details of the classification schemes are provided in the Supporting Information (Figures S5 and S6) and
180 in previous works (Moffet et al., 2012; Tomlin et al., 2020).

Scanning transmission X-ray microscopy with near edge X-ray absorption fine structure (STXM/NEXAFS) spectroscopy was used
to elucidate the chemical mixing state of individual particles based on the NEXAFS spectral data acquired at the Carbon K-edge
(278–320 eV) (Hopkins et al., 2007; Moffet et al., 2010b, c). The STXM/NEXAFS was performed at the synchrotron facilities on
beamlines 11.0.2.2 and 5.3.2.2 in the Advance Light Source, Lawrence Berkeley National Laboratory and on beamline 10ID-1 in
185 the University of Saskatchewan, Canadian Light Source. STXM instrument operation is similar in both locations as described
elsewhere (Kilcoyne et al., 2003). Briefly, a set of raster scan STXM images at each of the pre-set energy levels was acquired from
a synchrotron monochromated incident light focused on the sample using a Fresnel zone plate. The transmitted light is detected at
each of the energy settings, and spectra of individual particles could then be reconstructed based on the Beer-Lambert law from
the intensity of transmitted light over the projection area of particles compared to the particle-free regions. The recorded intensity
190 at each energy setting (E) across individual pixels were converted into optical density (OD_E) as follows:

$$OD_E = -\ln\left(\frac{I(E)}{I_0(E)}\right) = \mu\rho t \quad (1)$$

where $I(E)$ is the intensity of light transmitted through a particle, $I_0(E)$ is the intensity of incoming light (determined as intensity
of light in the particle-free areas), μ is the mass absorption coefficient, ρ corresponds to the density, and t is the thickness of a
particle. Sequences of STXM images are acquired at closely spaced energies of $I_0(E)$ to record a “stack” of images. Then, NEXAFS
195 spectra from individual pixels of detected particles are extracted from the stack (~96 energies over 278 to 320 eV range, 30–35 nm
spatial resolution, 1 ms dwell time).

In addition, faster acquisition of STXM images at four key energies of 278 eV (pre-edge), 285.4 eV (C=C), 288.5 eV (-COOH), and 320 eV (post-edge) (15x15 μm , 30–35 nm spatial resolution, 1 ms dwell time) was employed to construct “maps” of individual particles using image processing methods reported in our earlier studies (Moffet et al., 2010a, 2013, 2016; Fraund et al., 2017). Briefly, a series of thresholds were used to identify the mapping components including “inorganics” (IN), “organic carbon” (OC), and “soot/elemental carbon” (EC). The total carbon (TC) was calculated as the difference between the carbon post-edge and pre-edge OD ($\text{TC} = \text{OD}_{320\text{eV}} - \text{OD}_{278\text{eV}}$). “IN” rich regions were defined with pixels having an $\text{OD}_{278\text{eV}} / \text{OD}_{320\text{eV}}$ ratio greater than 0.5. “OC” regions are those with the abundant features corresponding to carboxylic acid functional group (-COOH), defined by the difference between intensity of the -COOH peak and carbon pre-edge peak greater than 0 (i.e., $\text{OD}_{288.5\text{eV}} - \text{OD}_{278\text{eV}} > 0$). Finally, EC areas are identified by comparing the value of the $\text{sp}^2/\text{total carbon}$ to that of highly oriented pyrolytic graphite (HOPG) according to: $(\text{OD}_{285.4\text{eV}}/\text{TC}) * (\text{OD}_{\text{HOPG, TC}}/\text{OD}_{\text{HOPG, C=C}}) > 0.35$, which indicates extensive sp^2 bonding of carbon corresponding to graphitic-like components (Hopkins et al., 2007).

3 Results and Discussion

3.1 Identification of dry intrusion periods

Research flights were conducted under different synoptic conditions to allow for the characterization of common aerosols, trace gases, clouds, and precipitation. Figure 1A illustrates the typical flight pattern of the G-1 aircraft which includes multiple legs at different altitudes, while maneuvering perpendicular and along the wind direction. These patterns allowed for the full profile of aerosol and cloud layer along the MBL and lower FT altitudes. Figure 1B shows daily time series between 2018-01-01 to 2018-02-28 in relation to DI events identified from ERA-Interim reanalysis. The marked black dots indicate DI air masses within a 3° radius from 39°N , 28°W (i.e., the ENA site). The high frequency of the black dots (i.e., vertical distribution) indicates an increase in trajectories that satisfy the DI criterion at different pressure altitudes. For example, on 2018-01-24 in Figure 1B, we see a series of DI air parcels (black dots) at different pressure altitudes ranging from 611 m to 2360 m MSL and found to be below/above the boundary layer as indicated by the dashed red line. Guided by the frequency of the DI air masses, we selected a subset of the time-tagged particle samples for analysis by the complementary microscopy techniques as summarized in Table S1. To evaluate the consistency of the sources and long-range transport trajectories, we calculated back trajectories using the HYSPLIT model (Stein et al., 2015; Rolph et al., 2017). Figure 1C shows results of a representative HYSPLIT 72 hrs back trajectory calculations for the research flight on 2018-01-24, which identifies long-range transport an air mass originating from North America. Trajectories were calculated every 6 hrs from 1300 UTC 2018-01-24 to 1200 UTC 2018-01-22 at 3 starting altitudes: 100 m, 2000 m, and 3000 m. This process was repeated with the same HYSPLIT input meteorological parameters for all research flights utilized in this work, as shown in Figures S1 and S2.

3.2 Particle-type classification

A total of 38 particle sample grids from 13 (out of 19) research flights were analyzed. First, CCSEM/EDX analysis was carried out to characterize the particle-type composition typical of different synoptic scenarios. Figure 2 shows the results of the size-segregated particle-type population (right column) obtained from k -means clustering analysis of ~36,400 individual particles with the backscattering mode SEM imaging of a representative subset of particles (left column), separated between MBL versus FT flight altitudes and between synoptic conditions of DI and non-DI sampling periods. The onboard FIMS instrument measurement provided particle size distribution data in a range of 0.01–0.5 μm . By superimposing the CCSEM/EDX particle analysis data with the FIMS size distribution data, we can approximate the representative composition and number concentration of potentially CCN active particles ($>0.1 \mu\text{m}$) in the MBL and FT, during non-DI and DI periods, respectively. Note that the error bars in the particle

235 number concentration indicate variation in the particle size distribution values averaged across different days and synoptic conditions. Also, comparison of AED and FIMS sizes needs to be considered with caution because particle fluttering on the substrate which results in overestimated of AED sizes, compared to more realistic FIMS values. Here, the AED based particle distributions are scaled to match Y-axis of FIMS data and therefore to provide visual illustration of the chemical makeup of CCN particles.

240 The *k*-means algorithm identified 4 key clusters and were termed as: “Carbonaceous”, “Ammonium Nitrates/Sulfates”, “Mixed Sea Salt” and “Aged Sea Salt” based on the mean elemental contribution (Figure S5). Note that the element fraction values obtained from individual EDX spectra were filtered to remove values less than 0.5%. “Carbonaceous” is the dominant type and represents majority of analyzed particles. It is defined based on the sole contributions of C- and O- elements in the particle EDX spectra. The second most abundant cluster is the “Ammonium Nitrates/Sulfates”, where the contribution of N, O, and S are greater than 1%.
245 The “Aged Sea Salt” and “Mixed Sea Salt” clusters contain similar elemental signatures with the latter containing significant amounts of refractory elements typical for sea salt and mineral dust including Mg, Cl, K, Ca, Mn, and Fe.

First, we compared the change in particle-type population among samples in the MBL during non-DI and DI periods. The fraction of “Carbonaceous” particles within the MBL contributed around 68% in non-DI samples and decreased to 43% in DI samples. Organic aerosol in the remote MBL has been suggested to originate from VOCs such as isoprenes, monoterpenes, formic acid,
250 nitrogenated, and aliphatic organics released from biological activities near the sea surface, which undergo oxidation reactions leading to SOA formation (Facchini et al., 2008; Dall’Osto et al., 2012; Mungall et al., 2017). The lower fraction of “Carbonaceous” particles during DI periods is counterbalanced by the increased of “Inorganics” shifting from 32% (non-DI periods) to 57% (DI periods). Here, we operationally defined “Inorganics” as the sum of “Mixed Sea Salt” (4%) + “Aged Sea Salt” (20%) + “Ammonium Nitrate/Sulfate” (33%), which in fact may also contain organic carboxylic acids as components of aged sea salt.
255 Regardless, shifting focus to the comparison of FT samples during non-DI and DI periods, we found that background “Carbonaceous” particles contribute to around 92% (non-DI periods) and decreases to 46% (DI periods). Similar to MBL observations, the shift in “Carbonaceous” contribution can be attributed to an increase in “Inorganic” influence during DI events changing from 8% (non-DI periods) to 55% (DI periods). We observed that most of the “Inorganic” influence is originating from “Ammonium Nitrate/Sulfate” contributing between 32–33% during DI periods regardless of sampling altitude (MBL vs. FT). Both
260 “Carbonaceous” particles and “Ammonium Nitrate/Sulfate” can originate from ocean biological activity or anthropogenic sources. Typically, over marine areas, sulfate aerosol forms from oxidation of dimethyl sulfide (DMS), a common gas species emitted by biota. Sulfates are major components of accumulation mode particles in the remote marine environment (Sanchez et al., 2018; Korhonen et al., 2008). Nitrate in marine particles can also come from vertical mixing in the ocean that surges nitrate-rich deep waters to the surface, followed by the aerosolization through wave motion (Zehr and Ward, 2002). However, the elevated
265 contribution of “Ammonium Nitrates/Sulfates” during the DI periods suggests likely influence from anthropogenic emissions originating from North America. Inorganic aerosols such as “Ammonium Nitrates/Sulfates” are predominantly formed from the condensation of atmospheric precursors such as SO₂, NH₃, HO_x, and NO_x, which are common components of biomass burning emissions, urban areas, and agriculture activities among others (Reff et al., 2009). A study utilizing regional chemical models have found that the mass enhancements in inorganic aerosol can reach 23% of carbonaceous enhancements as biomass burning processes
270 accelerate secondary formation of inorganic aerosols (Souri et al., 2017). Uptake of S- and N-containing acidic species, as well as soluble organic acids, onto the preexisting sea salt particles modifies their composition through acid-displacement reactions that can be expressed in a general form of (Finlayson-Pitts, 2003; Laskin et al., 2012):



where *NaCl denotes seasalt, HA represents atmospheric water-soluble acids (e.g., HNO₃, H₂SO₄, CH₃SO₃H and carboxylic acids).
275 These reactions release volatile HCl_(g) product, leaving particles depleted in chloride and enriched in corresponding HA_(aq) salts. Related to this acid-displacement chemistry “Mixed Sea Salt” and “Aged Sea Salt” particle-types were identified by the *k*-clustering analysis as illustrated in Figure S5. The “Mixed Sea Salt” particles contain key components of seawater (i.e., Na, Mg, and Cl; atomic fractions of Na and Cl >10% with characteristic ratio of Cl/Na ~0.6) and minor fractions (<2%) of additional elements (e.g., Ca, Mn, Fe, Al, and Si) suggesting internal mixing of relatively fresh sea salt with other inorganic components without extensive
280 chloride depletion. The other cluster of “Aged Sea Salt” particles shows significant fractions of Na (~10%), but with substantially lower ratios of Cl/Na <0.1 which indicates chloride depletion (Figure S5) due to atmospheric ageing. Atomic fractions of C and N elements in this type of particles are much higher than those in the “Mixed Sea Salt” cluster, while the fraction of S is much smaller. These observations suggest that in this geographical region acid-displacement reactions in the “Aged Sea Salt” particles are mostly driven by water-soluble carboxylic acids (common components of SOA) (Laskin et al., 2012) and nitric acid (Finlayson-Pitts,
285 2003), while contributions by sulfonic or sulfuric acids are minor during the wintertime. Based on the *k*-means clustering, fractions of “Mixed Sea Salt” range from 0.5 to 3% while fractions of “Aged Sea Salt” are overall more populous and range between 0.1 and 20% across all investigated samples. Additionally, both “Aged Sea Salt” and “Mixed Sea Salt” cluster groups include minor contributions of Al and Si indicative of possible mixing with mineral dust transported from the long-range continental sources.

To better discriminate particle-type groups according to their composition and the acid-displacement chemistry identified through
290 the *k*-means clustering, a supplemental rule-based classification was performed using previously published definitions of particle-type classes common in marine environments (Laskin et al., 2012; Tomlin et al., 2020). Results of the particle-type characterization utilizing the rule-based assessment of their elemental composition (assigned into 5 major classes) are presented in Figure S6. The applied rule-based classification scheme distinguishes among particle-types common in the remote marine environment of “Sea Salt”, “Sea Salt/Sulfate”, “Carbonaceous/Sulfate”, “Carbonaceous”, and “Other” (Figure S6). For each sample, 600–3000 particles
295 were analyzed, depending on particle loading on the substrates. The size-resolved particle-type classification identified using rule-based schematic were overlaid on the acquire FIMS size distribution as shown in Figure S7. Similar to the *k*-means clustering break down, we first compared the impact of DI events in MBL samples. Significant fractions of “Carbonaceous” and “Carbonaceous/Sulfate” particles were identified in the background MBL samples amounting to 86% (non-DI periods) while decreasing to 49% (DI period). Furthermore, the combined fraction of “Sea Salt” and mixed “Sea Salt/Sulfate” are substantially
300 smaller around 10% (non-DI periods) to 21% (DI period). Fractions of uncategorized “Other” particles contributes to around 30% (DI period) while only having minimal contribution of 4% during non-DI events. In contrast, background FT samples were dominated by “Carbonaceous” and “Carbonaceous/Sulfate” contributing to as high as 95% (non-DI periods) then decreasing to 55% (DI period). Unlike the MBL samples, there were only minimal change in larger “Sea Salt” + mixed “Sea Salt/Sulfate” from 2% (non-DI period) to 4% (DI period). However, the reduction in “Carbonaceous” and “Carbonaceous/Sulfate” contribution
305 among FT samples during DI periods is due to associated with the large change in “Other” fraction shifting from 4% (non-DI period) to 41% (DI period). Based on the mean elemental composition of the “Other” category, this group contains a combination of dust, sea salt, and carbonaceous components suggesting extensive internal mixing of particles consistent with long-range transport (Froyd et al., 2019). This finding is also consistent with the *k*-means clustering results that indicated elevated contributions of particles with inorganic components during the DI periods. Overall, the particle-type fraction identified by both the *k*-means
310 clustering and the rule-based classification schemes are consistent across all samples suggesting that the mixing state population significantly changes from heavily organic dominated to a mixture of inorganic-organic particle-type distribution resulting in the observation of more complex particle compositions during DI periods.

Relative contributions of the particle-type fractions among separate DI events show substantial variability between different flights and MBL versus FT altitudes (Figure S8). Furthermore, the dominant “Carbonaceous” particle-type groups identified by CCSEM/EDX elemental analysis may exhibit significant differences in the spectral characteristics of carbon bonding indicative of its long-range transport from North America during the DI periods. Furthermore, a previous study have tracked the origin of air masses transported over long distances across the Atlantic Ocean to the Azores utilizing a Lagrangian Flexible Particle (FLEXPART) dispersion model to show detailed spatial resolution of air masses across different locations and altitudes (China et al., 2017). The influence of North American emissions on distant remote regions is well documented with occurrences of continental pollutant transport events accompanied by strong influence from urban city emissions spanning from Boston, Toronto, Detroit, and Chicago (Owen et al., 2006). On the other hand, extensive boreal wildfires in northern North America release large amounts of trace gases and aerosols into the atmosphere, which then can be transported to other remote regions including North America (Val Martín et al., 2006). In particular, boreal wildfires emit around 10% of the annual anthropogenic aerosol black carbon in the Northern Hemisphere (Bond et al., 2004). The eastward transport of North American emissions begins as hot plumes of biomass burning emissions from wildfires rapidly rise to high altitudes (~8 to 13 km AGL) under favorable conditions (Zhu et al., 2018; Yu et al., 2019; Kloss et al., 2019). These plumes can be lofted into a warm conveyor belt preceding a cold front from an associated cyclone, which is followed by the entrainment of a cold descending air stream (from the same cyclone) that ultimately results in the air parcels containing continental emissions reaching the lower altitudes of the Eastern North Atlantic (Owen et al., 2006; Zheng et al., 2020b). The transported aerosol undergoes substantial atmospheric ageing through photochemical reactions (Hems et al., 2021), gas-particle partitioning (Vakkari et al., 2018), and coagulation (Ramnarine et al., 2019) processes as it travels across the Atlantic ocean and descends into the MBL during the DI events.

3.3 Internal mixing of individual particles

Results of the elemental microanalysis of particles presented above provides statistics on broad particle classes identified and shows well the significant contribution of organic dominated particles in the region. However, CCSEM/EDX analysis is limited in providing detailed information on the carbon speciation within individual particles and other metrics of particle internal composition (chemical mixing state). To investigate chemical differences in the carbon components of particles we employed STXM/NEXAFS spectro-microscopy methods, which provide spatially resolved carbon bonding speciation and differentiate between EC and OC regions within individual particles (Moffet et al., 2010a, c). It is also worth mentioning that the definitions of “Carbonaceous” particles identified by CCSEM/EDX and described in the previous section is somewhat different from OC particles defined by STXM/NEXAFS. The former corresponds to the distribution of organics across a population of particles (i.e., external mixing) while the latter is related to the multi-component internal heterogeneity of individual particles (i.e., internal mixing). Figure 3A shows an illustrative carbon K-edge map of individual particles from one of the DI period samples (the cumulative map of all ~4,300 particles from all samples analyzed in this study is included in SI, Figure S9). The carbon K-edge composition map distinguishes 3 main components based on the spectral information (Moffet et al., 2010a) as described earlier: IN (blue), OC (green), and EC (red). Each pixel within an individual particle may contain either single or multiple components (i.e., components can overlap) that are grouped to yield 5 typical classes based on the internal mixing between OC, EC, and IN components: (1) IN, (2) OC-EC-IN, (3) OC-EC, (4) OC-IN, and (5) OC. The size-resolved histograms of these 5 classes superimposed with the onboard particle size distribution data measured by FIMS is shown in Figure 3B to highlight the organic/inorganic contributions within individual particles as a function of particle size. A mixture of organic and inorganic particles (OC-IN) appears to be the dominant class across all samples, contributing 40–76% to the total particle population. Furthermore, the consideration of multiple sources of EC from wildfires (Park et al., 2007), residential wood smoke (Allen and

Rector, 2020), agricultural burning (Liu et al., 2016; Holder et al., 2017), and urban emissions (Paredes-Miranda et al., 2013) in North America led us to expect large contribution of EC within our sample. However, OC-EC and OC-EC-IN particles contributed only 0.4–1.3% to the total particle population. EC/soot lifetime is primarily governed by its wet deposition rate, which is dependent on the particle's affinity to absorb water (Barrett et al., 2019). Freshly emitted soot particles are hydrophobic, however atmospheric processes can increase the hygroscopicity properties of soot particles through the accumulation of OH initiated oxidation of organics during long-range transport and atmospheric ageing (Dzepina et al., 2015) leading to decreased atmospheric lifetime of EC regardless of initial composition (Khalizov et al., 2013; Browne et al., 2015; China et al., 2015). IN particles (i.e., inorganics such as sea salt and sulfates) appear to be consistent with the particle-type observations inferred from CCSEM/EDX data. Single-component IN particles contribute up to 15% in the MBL at the time of no-DI periods, while their contribution during DI decreases to ~0.8%. Subject to long-range transport, IN dominant particles also accumulate substantial OC components encountering the DI, and as they entrain into the MBL and create ensembles of ambient particles with complex multi-component internal mixing states through different atmospheric processes such as condensation (Mozurkewich, 1986) and coagulation (Holmes, 2007). Consistently, fractions of single-component OC particles within the MBL during DI periods increased (from 7% to 22%) and slightly decreased in the FT layer (from 26% to 20%). These observations suggest that entrainment of aerosols with higher extents of internal mixing (from long-range transport) are present in the MBL and can contribute to the regional aerosol composition, which in turn may modify aerosol-cloud interactions typical for the area.

NEXAFS spectra (285–294 eV) of individual particles were used to assess carbon chemical bonding environment allowing us to identify representative types of OC containing particles (Moffet et al., 2010a). Figure 4 shows the representative NEXAFS spectra acquired over 103 individual carbon containing particles. This resulted in the identification of 6 carbon “types,” as shown along with their illustrative secondary electron mode SEM imaging. Each carbon “type” is classified based on characteristic spectral features such as peak positions and relative intensities. For all spectra shown in Figure 4A, the individual contribution of carbon energy transitions was quantified via spectral deconvolution. Details on the deconvolution process are described in previous works (Moffet et al., 2010b, 2013; Tomlin et al., 2020). Figure 5A shows the deconvolution fit of the averaged NEXAFS spectra for each carbon “type” identified across different sampling conditions with Figure 5B illustrating the contribution of each functional group based on the individual peak area. It is worth noting that the difference in absorption between the post-edge ($OD_{320\text{ eV}}$) and pre-edge ($OD_{278\text{ eV}}$) energies is a measure of the amount of total carbonaceous material in the particles.

“Type 1 – biological” class has some contribution from alkene groups ($C^*=C$ @ 285.4 eV) with significant enhancement of aliphatic hydrocarbons (C^*-H @ 287.7 eV) and alcohol groups (C^*-OH @ 289.5 eV). These spectra appear to be similar to the reported NEXAFS spectrum for phospholipids, a constituent of cell walls (Lawrence et al., 2003; Nováková et al., 2008). Lipid material is concentrated in the sea surface microlayer through the rupturing of phytoplankton cell membranes (i.e., cell lysis) (Wang et al., 2015b). A majority of lipid compounds produced by phytoplankton in seawater include glyceroglycolipids, phospholipids, and triacylglycerols containing significant amounts of aliphatic, and alcohol groups (Harwood and Guschina, 2009). The transition of aliphatic-rich organic species into the aerosol phase is governed by the bursting of bubble films (Blanchard, 1989) enriched in lipid organic species found on the surface of seawater (Wang et al., 2015b). “Type 2 – homogeneous organic particles” have almost equivalent peak contributions from each reported functional group as shown in Figure 5B. The NEXAFS spectrum for type 2 is quantitatively similar to those reported for organic particles from anthropogenic emissions in urban areas of Mexico City (Moffet et al., 2010b) and Central California (Moffet et al., 2013). As the aerosol plume is transported away from the source of emission, organic mass increases while the fraction of $C=C$ decreases (Doran et al., 2007; Kleinman et al., 2008; Moffet et al., 2010b). As a result, organic functional groups build up with particle age such as carboxylic acids, carbonyl, alcohol, and other carbon–oxygen functional groups. It has been suggested that formation of these homogeneous organic particles likely results from

the accumulation growth of primary emitted particles as they traveled further way from their emission source (Moffet et al., 2010b). “Type 3 – soot” had the largest contribution of C*=C @ 285.4 eV spectral feature (42% of peak area contribution). Based on reported literature, this spectrum is comparable with atmospheric particles collected during various field studies of biomass burning emissions (Hopkins et al., 2007). Interestingly, particles collected from aircraft measurements during the Aerosol Characterization Experiment in Asia (ACE-Asia) campaign (Maria et al., 2004) from emissions over mixed combustion sources had near identical % sp² value around 41% (Hopkins et al., 2007).

Field and laboratory studies showed that sea salt particles can react with atmospheric water-soluble organic acids leading to chloride depletion within particles (Laskin et al., 2012; Wang et al., 2015a). Consistent with these previous studies, fresh sea salt typically has an intact rectangular inorganic core with a carbon outer shell arising from a thin layer of carboxylic acid coating as indicated by the peak for R(C*=O)OH @ 288.5 eV. Accordingly, “Type 4” is referred to as “fresh sea salt” in this work. In addition, the minor quantity of carbonaceous material in Type 4, as inferred from the small difference between the post- and pre-edge energies (OD_{320 eV} – OD_{278 eV}) apparent from Figure 5A, further supports the observation of freshly emitted sea salt particles. In contrast, “Type 5 – aged sea salt/organics” are sea salt particles that have reacted with carboxylic acid components of organic aerosol condensate which results in a substantial contribution of the R(C*=O)OH @ 288.5 eV peak while retaining the carbonate peak C*O₃ @ 290.4 eV. Of note, “Type 5 – aged sea salt/organics” contain significantly more carbon mass than “Type 4–fresh sea salt/organics,” as indicated by their NEXAFS spectrum. Finally, “Type 6 – K dominated” class is identified based on the appearance of characteristic potassium peaks at 297.1 eV (K*_{L2}), and 299.7 eV (K*_{L3}) with a percent contribution of ~51% relative to the total peak area. Potassium-salt particles are common markers of biomass burning smoke (Andreae, 1983; Li et al., 2003). Large fractions of KCl particles are commonly emitted from both flaming and smoldering fires, while atmospheric ageing can transform them into K₂SO₄ and KNO₃ through multi-phase acid displacement reactions similar to those of NaCl (Li et al., 2003). However, these K dominated particles can also be release as mixed secondary particles containing fractions of organic species, methylsulfonic acid, trimethylamine, SO₄²⁻, NH₄⁺, and K from potential biogenic sources in oceans (Willis et al., 2017).

3.4 Organic volume fraction of individual mixed organic-inorganic particles

Organic volume fraction (OVF) is a practical parameter to assess reactivity (Worsnop et al., 2002; Folkers et al., 2003) and hygroscopicity (Wang et al., 2008; Schill et al., 2015; Ruehl et al., 2016) of mixed inorganic–organic particles. Based on the STXM/NEXAFS measurements of individual particles, OVF is defined as a ratio of the optical thickness of the organic components (t_{org}) divided by the total optical thickness of the particle ($t_{org} + t_{inorg}$) (Moffet et al., 2010a; Pham et al., 2017; Fraund et al., 2019). STXM images collected at the carbon K-edge were used to calculate the OVF. The values of absorbance at the pre-edge (278 eV) and the post edge (320 eV) energies are related to the inorganic mass and the sum of inorganic + organic mass, respectively. Assuming specific values for densities (ρ) and mass absorption coefficients (μ) for the organic and inorganic components, values of t_{org} and t_{inorg} can be determined, allowing OVF calculation (Fraund et al., 2019). For this study, we assumed the inorganic component of particles corresponds to (NH₄)₂SO₄ based on the particle elemental composition identified by CCSEM/EDX analysis, while oxalic acid (C₂H₂O₄) is used as a proxy for the organic component. Oxalic acid was chosen to represent biomass burning (Yamasoe et al., 2000) and vehicular exhaust (Kawamura and Kaplan, 1987). Of note, based on previous reported studies, assumptions of chemically different organic components has minor effect on the resulting OVF values, while choice of the inorganic components resulted in a larger variation in the OVF calculations (Pham et al., 2017; Fraund et al., 2019). Here, we estimate the systematic error in OVF when assuming different inorganic-organic components, as shown in Table S2. Assuming NaCl to be the inorganic component instead of (NH₄)₂SO₄ yields a difference of ~35%. On the other hand, assuming

430 the organic component to be oxalic acid yields a ~5–30% difference in OVF when compared to other organics depending such as sucrose, adipic acid, and glucose.

Figure 6 shows representative chemical mixing state maps and OVF values of particles sampled during different atmospheric transport episodes during this study. Particles appear to have varying amount of organic coating for different sampling episodes as shown in the OVF maps. The comparison of the OVF map and the carbon speciation map illustrates overlap between the two mapping schemes. Finally, histograms show particle fractions at varying OVF values during different atmospheric transport episodes. Layers of organics are seen encapsulating inorganic cores. As expected, background particles collected in the MBL show inorganic NaCl cores (as indicated by a rectangular core morphology) with modest organic coating (OVF <30%), consistent with a previous report (Chi et al., 2015). However, during the DI periods, the majority of particles have equal or greater fractions of organic to inorganic components (40–60% OVF), while only a few particles exhibit core/shell morphology typical for background particles (i.e., non-DI periods). Furthermore, FT particles during non-DI periods have OVF <10%, when compared to FT samples during DI periods (10–20% OVF). In general, samples collected at the FT altitudes show reduced OVF values compared to the MBL samples regardless of the occurrence of DIs. Core-shell particle morphologies were also observed in FT sample, albeit not frequently (see Figure S9). FT samples were dominated by inorganic-organic particles in the size range of 0.20–0.25 μm , which are likely mixed sulfate-organic particles based on the size-resolved particle-type datasets obtained from CCSEM/EDX analysis. A recent study conducted in central Oregon found that the organic mass fraction from FT samples were between 27–84% while sulfate mass fractions were ranging from 39–50% (Zhou et al., 2019). Based on these reported studies the elevated contributions of organic and sulfate in the FT may be attributed to the enrichment of organonitrates and organosulfate compounds originating from biogenic sources in the absence of wildfire influence. However, FT organic and sulfate aerosol mass is also known to be associated with urban and biomass burning emissions (Bahreini, 2003; Dunlea et al., 2009; Roberts et al., 2010; Wang et al., 2021b). Studies in the northeast Pacific found that submicron aerosol mass was dominated by sulfate and organic components originating from aged Asian pollution plumes (Dunlea et al., 2009). FT organic and sulfate particles can then experience long-range transport and ageing as the air parcels are carried across the Atlantic and descend into the MBL of the ENA site (China et al., 2017). To summarize, we observe enhancements in the OVF values of individual particles during the DI periods, quantified as 2.06 ± 0.16 and 1.11 ± 0.04 fold increase of OVF for the MBL and FT samples, respectively, assuming $(\text{NH}_4)_2\text{SO}_4$ -oxalic acid components. The larger total OVF in the MBL (relative to FT samples) regardless of DI events is most likely due to additional contribution of marine organic sources within the boundary layer. The background organic concentration in the MBL is different than FT due to other sources of organics such as dissolved organic matter on the seawater surface (Doval et al., 2001; Miyazaki et al., 2018). The transport of organics from the ocean surface directly into the atmosphere is primary driven by turbulent winds (O'Dowd et al., 2004; Prather et al., 2013) resulting in the enhancement in the background organic concentration in the MBL. Furthermore, the observed enhancements in OVF in the MBL during DI periods could be the result of organic-rich air parcels (originating from North America) descending from the FT into the MBL leading to changes in total organic concentration (Zheng et al., 2020b; Wang et al., 2021b).

3.5 Evaluating CCN activity of mixed organic-inorganic particles

CCN activity of individual particles is governed by both their size and chemical composition. In particular, condensation of organic carbon onto atmospheric inorganic particles can impact the efficiency at which particles of mixed organic-inorganic composition can act as CCN and INP due to changes in particles' hygroscopicity and viscosity (Beydoun et al., 2017; Ovadnevaite et al., 2017; Altaf et al., 2018). To account for the effects of organics on aerosol hygroscopicity, we use κ -Köhler equation (Petters and Kreidenweis, 2007) to estimate the hygroscopicity parameter κ corresponding to mixed inorganic-organic particles:

$$\kappa = (1 - f_{\text{org}}) \kappa_{\text{inorg}} + f_{\text{org}} \kappa_{\text{org}} \quad (2)$$

470 where, f_{org} is the OVF values derived from the STXM data, $\kappa_{\text{org}} = 0.1$ is the hygroscopicity of the organic component, and $\kappa_{\text{inorg}} = 0.6$ is that of $(\text{NH}_4)_2\text{SO}_4$ (Petters and Kreidenweis, 2007). We derived κ values for different synoptic and atmospheric layer conditions using the size-resolved OVF ratio shown in Figure S10, and found that $\kappa_{\text{MBL, DI}} = 0.41$ and $\kappa_{\text{FT, DI}} = 0.33$ for DI periods, and $\kappa_{\text{MBL, non-DI}} = 0.48$ and $\kappa_{\text{FT, non-DI}} = 0.36$ for non-DI periods. The lower κ values under DI periods are consistent with enhancements in the organic contribution. Of note, the values of κ obtained here using Eq. 2 needs to be considered as the low
475 limit values, which might be somewhat higher considering possible contributions from more hygroscopic components of particles related to original and aged sea salt ($\kappa_{\text{NaCl}} = 1.3$ and $\kappa_{\text{Na}_2\text{SO}_4} = 0.8$).

Using κ , we can calculate the critical size of a dry particle (Figure S11) that can be activated under the supersaturation of 0.14% (setting of the CCN counter deployed on G-1) (Petters and Kreidenweis, 2007). The theoretical CCN number concentrations are then estimated by integrating the FIMS-measured aerosol size distributions above the critical dry particle diameter. Figure 7 shows
480 the results for the OVF-based calculations of theoretical CCN concentrations compared to the onboard CCN measurements at 0.14% supersaturation. There is a general agreement between calculated and measured CCN concentration, but FT cases appear to have a better agreement. The uncertainty in the calculated CCN is due to the supersaturation fluctuation of the CCN counter (0.13–0.15%), as shown in Figure S11. The large error bars in the measured CCN are a result of the variability of the measured CCN during different sampling periods. We also note that the exact value of κ_{org} may play a role in affecting the CCN calculation. So,
485 theoretical CCN concentrations were also calculated using $\kappa_{\text{org}} = 0$, and the results were compared against the measured CCN concentrations in Fig. 7b. However, the impact of this change of κ_{org} does not significantly change the agreement between the calculated and measured CCN concentrations. This result shows that calculating the CCN concentration using OVF values derived from the STXM data and the κ -Köhler theory can be a good estimate of the actual CCN concentrations.

4 Conclusion

490 Here, we presented detailed chemical imaging of individual atmospheric particles collected over the Azores during long-ranged transport events. Air mass back trajectory calculations suggest that air parcels in the ENA region can be traced from more than 4000 km away from North America within a span of 48-72 hours. During these long-range transport episodes, aerosols undergo substantial changes in size, morphology, and chemical composition among others as they are carried across the Atlantic Ocean and descend from the FT into the MBL altitudes over the ENA region. Chemical composition of elements of individual particles
495 (~36,400) were quantified using CCSEM/EDX while a subset of particles (~4,300) was analyzed using STXM/NEXAFS to determine the particle internal mixing state and organic spatial distribution. Based on CCSEM/EDX analysis, we observe a substantial contribution of “Carbonaceous” particles which are the dominant particle-type across all samples. The fraction of externally mixed “Carbonaceous” particles decreases during the DI periods, compensated by the increase of “Ammonium Nitrate/Sulfate” fraction. The elevated contribution of atmospheric nitrate suggests influence from anthropogenic and biomass
500 burning emissions (Reff et al., 2009). This observation is consistent with the DI periods suggesting air masses originating from North America descend from FT to MBL over the ENA region. Interestingly, there is also an increase in particle-type diversity in the FT during DI periods most likely due to significant mixing during DI episodes based on measured particle number concentrations. Among these identified “Carbonaceous” particles, the OVF across individual particles derived from STXM measurements is enhanced in DI samples. Aged aerosols accumulate organics through condensation of secondary semi-volatile
505 species resulting in an increase in organic contribution among individual particles. We utilize the STXM-derived OVF values and implemented it into the calculation of particle hygroscopicity using κ -Köhler theory (Petters and Kreidenweis, 2007). Particles

collected during DI periods resulted in lower κ value with respect to background marine aerosols common in the ENA region resulting in reduced CCN propensity. We calculated κ values between ~0.29 and ~0.44 corresponding to mixed organic-inorganic aerosol in the FT and MBL, respectively. These values are consistent with previous reported studies on mixed organic particles (Petters and Kreidenweis, 2007; Schmale et al., 2018; Zheng et al., 2020b).

Current atmospheric models lack the representation of aerosol mixing states limiting to only simple assumptions leading to high uncertainty of aerosol impact on the Earth's system. It is traditionally assumed that sulfate particles dictate particle growth over remote ocean regions while underestimating the influence of organic particles on the CCN activity over remote oceans. We have shown that particles transported from North America can have a substantial impact on the aerosol mixing state and aerosol population over the region of study, as organic contribution and particle-type diversity is significantly enhanced during the DI periods. These observations need to be considered in current atmospheric models to have a better predictive understanding of the impact of long-range transport episodes to the source apportionment of specific aerosol particle types and the extent of particle internal heterogeneity.

Supplement

The supplement related to this article is available online at:

Author Contribution

D.V., S.C., D.K., R.M., J. Wang and A.L. designed the study. D.V., J.S. and J. Wang executed sample collection and data acquisition during field deployment. S.R.-R. performed modeling tasks of the study. J.T., K.J., D.V., S.C., P.W., M.F., J. Weis, F.R.-A., D.K., R. C., M.G. performed chemical imaging experiments and analyzed associated data. G.Z., Y.W. and J. Wang analyzed real-time data from G-1. J.T. and A.L. wrote the manuscript with contributions from all coauthors.

ORCID

Jay M. Tomlin: [0000-0002-3081-1512](https://orcid.org/0000-0002-3081-1512)

Kevin A. Jankowski: [0000-0003-4640-5161](https://orcid.org/0000-0003-4640-5161)

Daniel P. Veghte: [0000-0001-7422-7791](https://orcid.org/0000-0001-7422-7791)

Swarup China: [0000-0001-7670-335X](https://orcid.org/0000-0001-7670-335X)

Matthew Fraund: [0000-0002-7460-4283](https://orcid.org/0000-0002-7460-4283)

Guangjie Zheng: [0000-0002-8103-2594](https://orcid.org/0000-0002-8103-2594)

Yang Wang: [0000-0002-0543-0443](https://orcid.org/0000-0002-0543-0443)

Felipe A. Rivera-Adorno: [0000-0002-7355-7999](https://orcid.org/0000-0002-7355-7999)

Shira Raveh-Rubin: [0000-0001-6244-8693](https://orcid.org/0000-0001-6244-8693)

John Shilling: [0000-0002-3728-0195](https://orcid.org/0000-0002-3728-0195)

Daniel Knopf: [0000-0001-7732-3922](https://orcid.org/0000-0001-7732-3922)

Ryan C. Moffet: [0000-0002-2352-5454](https://orcid.org/0000-0002-2352-5454)

Mary K. Gilles: [0000-0002-0672-3117](https://orcid.org/0000-0002-0672-3117)

Jian Wang: [0000-0002-2815-4170](https://orcid.org/0000-0002-2815-4170)

Alexander Laskin: [0000-0002-7836-8417](https://orcid.org/0000-0002-7836-8417)

Competing Interests

The authors declare that they have no conflict of interest.

Acknowledgements

545 We would like to thank the ACE-ENA campaign team for their help and support. The research funded by the Atmospheric System
Research (ASR) program, Office of Biological and Environmental Research (OBER) of the United States Department of Energy,
awards No. DE-SC0018948 (Purdue/STI group), DE-SC0020259 (Washington University), SC0016370 and SC0021034 (Knopf
group), SR-R acknowledges funding from the Israel Science Foundation (grant No. 1347/18). The research used STXM/NEXAFS
550 instruments at beamline 5.3.2.2 and 11.0.2 at the Advance Light Source at Lawrence Berkeley National Laboratory with the
guidance from David Kilcoyne, Matthew Markus, Hendrik Ohldag, and David Shapiro. In addition, the soft X-ray
spectromicroscopy 10ID-1 beamline at the Canadian Light Source was also used in this study, assisted by the beamline scientist
Jian Wang. We used CCSEM/EDX instrument at Environmental Molecular Sciences Laboratory located at the Pacific Northwest
National Laboratory. We thank John Shilling for providing the data collected from the Aerodyne HR-ToF-AMS onboard the G-1
555 aircraft during the ACE-ENA campaign. The authors gratefully acknowledge the NOAA Air Resources Laboratory (ARL) for the
provision of the HYSPLIT transport and dispersion model and/or READY website (<https://www.ready.noaa.gov>) used in this
publication.

Financial Support

U.S. Department of Energy Atmospheric System Research program, award DE-SC0018948.

560

Reference

- Ackerman, A. S., Kirkpatrick, M. P., Stevens, D. E., and Toon, O. B.: The impact of humidity above stratiform clouds on indirect aerosol climate forcing, *Nature*, 432, 1014–1017, <https://doi.org/10.1038/nature03174>, 2004.
- 565 Adachi, K., Oshima, N., Gong, Z., de Sá, S., Bateman, A. P., Martin, S. T., de Brito, J. F., Artaxo, P., Cirino, G. G., Sedlacek III, A. J., and Buseck, P. R.: Mixing states of Amazon basin aerosol particles transported over long distances using transmission electron microscopy, *Atmos. Chem. Phys.*, 20, 11923–11939, <https://doi.org/10.5194/acp-20-11923-2020>, 2020.
- Allen, G. and Rector, L.: Characterization of Residential Woodsmoke PM_{2.5} in the Adirondacks of New York, *Aerosol Air Qual. Res.*, 20, 2419–2432, <https://doi.org/10.4209/aaqr.2020.01.0005>, 2020.
- 570 Altaf, M. B., Dutcher, D. D., Raymond, T. M., and Freedman, M. A.: Effect of Particle Morphology on Cloud Condensation Nuclei Activity, *ACS Earth Space Chem.*, 2, 634–639, <https://doi.org/10.1021/acsearthspacechem.7b00146>, 2018.
- Altartz, O., Koren, I., Remer, L. A., and Hirsch, E.: Review: Cloud invigoration by aerosols—Coupling between microphysics and dynamics, *Atmos. Res.*, 140–141, 38–60, <https://doi.org/10.1016/j.atmosres.2014.01.009>, 2014.
- Andreae, M. O.: Soot Carbon and Excess Fine Potassium: Long-Range Transport of Combustion-Derived Aerosols, *Science*, 220, 1148–1151, <https://doi.org/10.1126/science.220.4602.1148>, 1983.
- 575 Andreae, M. O., Ferek, R. J., Bermond, F., Byrd, K. P., Engstrom, R. T., Hardin, S., Houmère, P. D., LeMarrec, F., Raemdonck, H., and Chatfield, R. B.: Dimethyl sulfide in the marine atmosphere, *J. Geophys. Res.*, 90, 12891, <https://doi.org/10.1029/JD090iD07p12891>, 1985.
- Ault, A. P., Gaston, C. J., Wang, Y., Dominguez, G., Thiemens, M. H., and Prather, K. A.: Characterization of the Single Particle Mixing State of Individual Ship Plume Events Measured at the Port of Los Angeles, *Environ. Sci. Technol.*, 44, 1954–1961, <https://doi.org/10.1021/es902985h>, 2010.
- 580 Ault, A. P., Peters, T. M., Sawvel, E. J., Casuccio, G. S., Willis, R. D., Norris, G. A., and Grassian, V. H.: Single-Particle SEM-EDX Analysis of Iron-Containing Coarse Particulate Matter in an Urban Environment: Sources and Distribution of Iron within Cleveland, Ohio, *Environ. Sci. Technol.*, 46, 4331–4339, <https://doi.org/10.1021/es204006k>, 2012.
- Ault, A. P., Moffet, R. C., Baltrusaitis, J., Collins, D. B., Ruppel, M. J., Cuadra-Rodriguez, L. A., Zhao, D., Guasco, T. L., Ebben, C. J., Geiger, F. M., Bertram, T. H., Prather, K. A., and Grassian, V. H.: Size-Dependent Changes in Sea Spray Aerosol Composition and Properties with Different Seawater Conditions, *Environ. Sci. Technol.*, 47, 5603–5612, <https://doi.org/10.1021/es400416g>, 2013.
- Bahreini, R.: Aircraft-based aerosol size and composition measurements during ACE-Asia using an Aerodyne aerosol mass spectrometer, *J. Geophys. Res.*, 108, 8645–8658, <https://doi.org/10.1029/2002JD003226>, 2003.
- 590 Barrett, T. E., Ponette-González, A. G., Rindy, J. E., and Weathers, K. C.: Wet deposition of black carbon: A synthesis, *Atmos. Environ.*, 213, 558–567, <https://doi.org/10.1016/j.atmosenv.2019.06.033>, 2019.
- Beydoun, H., Polen, M., and Sullivan, R. C.: A new multicomponent heterogeneous ice nucleation model and its application to Snomax bacterial particles and a Snomax–illite mineral particle mixture, *Atmos. Chem. Phys.*, 17, 13545–13557, <https://doi.org/10.5194/acp-17-13545-2017>, 2017.
- 595 Blanchard, D. C.: The Ejection of Drops from the Sea and Their Enrichment with Bacteria and Other Materials: A Review, *Estuaries*, 12, 127–137, <https://doi.org/10.2307/1351816>, 1989.
- Bond, T. C., Streets, D. G., Yarber, K. F., Nelson, S. M., Woo, J.-H., and Klimont, Z.: A technology-based global inventory of black and organic carbon emissions from combustion, *J. Geophys. Res.*, 109, D14203 1–43, <https://doi.org/10.1029/2003JD003697>, 2004.
- 600 Bondy, A. L., Bonanno, D., Moffet, R. C., Wang, B., Laskin, A., and Ault, A. P.: The diverse chemical mixing state of aerosol particles in the southeastern United States, *Atmos. Chem. Phys.*, 18, 12595–12612, <https://doi.org/10.5194/acp-18-12595-2018>, 2018.

- Bony, S.: Marine boundary layer clouds at the heart of tropical cloud feedback uncertainties in climate models, *Geophys. Res. Lett.*, 32, L20806, <https://doi.org/10.1029/2005GL023851>, 2005.
- 605 Browne, E. C., Franklin, J. P., Canagaratna, M. R., Massoli, P., Kirchstetter, T. W., Worsnop, D. R., Wilson, K. R., and Kroll, J. H.: Changes to the Chemical Composition of Soot from Heterogeneous Oxidation Reactions, *J. Phys. Chem. A*, 119, 1154–1163, <https://doi.org/10.1021/jp511507d>, 2015.
- Browning, K. A.: The dry intrusion perspective of extra-tropical cyclone development, *Meteorol. Appl.*, 4, 317–324, <https://doi.org/10.1017/S1350482797000613>, 1997.
- 610 Buseck, P. R. and Posfai, M.: Airborne minerals and related aerosol particles: Effects on climate and the environment, *Proc. Natl. Acad. Sci.*, 96, 3372–3379, <https://doi.org/10.1073/pnas.96.7.3372>, 1999.
- Catto, J. L. and Raveh-Rubin, S.: Climatology and dynamics of the link between dry intrusions and cold fronts during winter. Part I: global climatology, *Clim. Dyn.*, 53, 1873–1892, <https://doi.org/10.1007/s00382-019-04745-w>, 2019.
- Chi, J. W., Li, W. J., Zhang, D. Z., Zhang, J. C., Lin, Y. T., Shen, X. J., Sun, J. Y., Chen, J. M., Zhang, X. Y., Zhang, Y. M., and Wang, W. X.: Sea salt aerosols as a reactive surface for inorganic and organic acidic gases in the Arctic troposphere, *Atmos. Chem. Phys.*, 15, 11341–11353, <https://doi.org/10.5194/acp-15-11341-2015>, 2015.
- China, S., Scarnato, B., Owen, R. C., Zhang, B., Ampadu, M. T., Kumar, S., Dzepina, K., Dziobak, M. P., Fialho, P., Perlinger, J. A., Hueber, J., Helmig, D., Mazzoleni, L. R., and Mazzoleni, C.: Morphology and mixing state of aged soot particles at a remote marine free troposphere site: Implications for optical properties, *Geophys. Res. Lett.*, 42, 1243–1250, <https://doi.org/10.1002/2014GL062404>, 2015.
- 620 China, S., Alpert, P. A., Zhang, B., Schum, S., Dzepina, K., Wright, K., Owen, R. C., Fialho, P., Mazzoleni, L. R., Mazzoleni, C., and Knopf, D. A.: Ice cloud formation potential by free tropospheric particles from long-range transport over the Northern Atlantic Ocean: Ice cloud formation by aged particles, *J. Geophys. Res. Atmospheres*, 122, 3065–3079, <https://doi.org/10.1002/2016JD025817>, 2017.
- 625 Cruz, C. N. and Pandis, S. N.: A study of the ability of pure secondary organic aerosol to act as cloud condensation nuclei, *Atmos. Environ.*, 31, 2205–2214, [https://doi.org/10.1016/S1352-2310\(97\)00054-X](https://doi.org/10.1016/S1352-2310(97)00054-X), 1997.
- Cubison, M. J., Ortega, A. M., Hayes, P. L., Farmer, D. K., Day, D., Lechner, M. J., Brune, W. H., Apel, E., Diskin, G. S., Fisher, J. A., Fuelberg, H. E., Hecobian, A., Knapp, D. J., Mikoviny, T., Riemer, D., Sachse, G. W., Sessions, W., Weber, R. J., Weinheimer, A. J., Wisthaler, A., and Jimenez, J. L.: Effects of aging on organic aerosol from open biomass burning smoke in aircraft and laboratory studies, *Atmos. Chem. Phys.*, 11, 12049–12064, <https://doi.org/10.5194/acp-11-12049-2011>, 2011.
- Dall’Osto, M., Ceburnis, D., Monahan, C., Worsnop, D. R., Bialek, J., Kulmala, M., Kurtén, T., Ehn, M., Wenger, J., Sodeau, J., Healy, R., and O’Dowd, C.: Nitrogenated and aliphatic organic vapors as possible drivers for marine secondary organic aerosol growth: Marine secondary organic aerosol growth, *J. Geophys. Res. Atmospheres*, 117, n/a-n/a, <https://doi.org/10.1029/2012JD017522>, 2012.
- 635 DeCarlo, P. F., Kimmel, J. R., Trimborn, A., Northway, M. J., Jayne, J. T., Aiken, A. C., Gonin, M., Fuhrer, K., Horvath, T., Docherty, K. S., Worsnop, D. R., and Jimenez, J. L.: Field-Deployable, High-Resolution, Time-of-Flight Aerosol Mass Spectrometer, *Anal. Chem.*, 78, 8281–8289, <https://doi.org/10.1021/ac061249n>, 2006.
- Dee, D. P., Uppala, S. M., Simmons, A. J., Berrisford, P., Poli, P., Kobayashi, S., Andrae, U., Balmaseda, M. A., Balsamo, G., Bauer, P., Bechtold, P., Beljaars, A. C. M., van de Berg, L., Bidlot, J., Bormann, N., Delsol, C., Dragani, R., Fuentes, M., Geer, A. J., Haimberger, L., Healy, S. B., Hersbach, H., Hólm, E. V., Isaksen, I., Kållberg, P., Köhler, M., Matricardi, M., McNally, A. P., Monge-Sanz, B. M., Morcrette, J.-J., Park, B.-K., Peubey, C., de Rosnay, P., Tavolato, C., Thépaut, J.-N., and Vitart, F.: The ERA-Interim reanalysis: configuration and performance of the data assimilation system, *Q. J. R. Meteorol. Soc.*, 137, 553–597, <https://doi.org/10.1002/qj.828>, 2011.
- 645 Doran, J. C., Barnard, J. C., Arnott, W. P., Cary, R., Coulter, R., Fast, J. D., Kassianov, E. I., Kleinman, L., Laulainen, N. S., Martin, T., Paredes-Miranda, G., Pekour, M. S., Shaw, W. J., Smith, D. F., and Springston, S. R.: The T1-T2 study: evolution of aerosol properties downwind of Mexico City, *Atmos Chem Phys*, 15, 1585–1598, <https://doi.org/10.5194/acp-7-1585-2007>, 2007.

- Doval, M. D., Álvarez-Salgado, X. A., and Pérez, F. F.: Organic matter distributions in the Eastern North Atlantic–Azores Front region, *J. Mar. Syst.*, 30, 33–49, [https://doi.org/10.1016/S0924-7963\(01\)00036-7](https://doi.org/10.1016/S0924-7963(01)00036-7), 2001.
- 650 Dunlea, E. J., DeCarlo, P. F., Aiken, A. C., Kimmel, J. R., Peltier, R. E., Weber, R. J., Tomlinson, J., Collins, D. R., Shinozuka, Y., McNaughton, C. S., Howell, S. G., Clarke, A. D., Emmons, L. K., Apel, E. C., Pfister, G. G., van Donkelaar, A., Martin, R. V., Millet, D. B., Heald, C. L., and Jimenez, J. L.: Evolution of Asian aerosols during transpacific transport in INTEX-B, *Atmos Chem Phys*, 31, 2009.
- 655 Dzepina, K., Mazzoleni, C., Fialho, P., China, S., Zhang, B., Owen, R. C., Helmig, D., Hueber, J., Kumar, S., Perlinger, J. A., Kramer, L. J., Dziobak, M. P., Ampadu, M. T., Olsen, S., Wuebbles, D. J., and Mazzoleni, L. R.: Molecular characterization of free tropospheric aerosol collected at the Pico Mountain Observatory: a case study with a long-range transported biomass burning plume, *Atmos. Chem. Phys.*, 15, 5047–5068, <https://doi.org/10.5194/acp-15-5047-2015>, 2015.
- ECMWF: Integrated forecasting system’s documentation, Part IV: Physical processes, (IFS Documentation CY31R1), 2007.
- 660 Facchini, M. C., Rinaldi, M., Decesari, S., Carbone, C., Finessi, E., Mircea, M., Fuzzi, S., Ceburnis, D., Flanagan, R., Nilsson, E. D., de Leeuw, G., Martino, M., Woeltjen, J., and O’Dowd, C. D.: Primary submicron marine aerosol dominated by insoluble organic colloids and aggregates, *Geophys. Res. Lett.*, 35, L17814, <https://doi.org/10.1029/2008GL034210>, 2008.
- Finlayson-Pitts, B. J.: The Tropospheric Chemistry of Sea Salt: A Molecular-Level View of the Chemistry of NaCl and NaBr, *Chem. Rev.*, 103, 4801–4822, <https://doi.org/10.1021/cr020653t>, 2003.
- 665 Folkers, M., Mentel, Th. F., and Wahner, A.: Influence of an organic coating on the reactivity of aqueous aerosols probed by the heterogeneous hydrolysis of N₂O₅: Organic coatings and aerosol reactivity, *Geophys. Res. Lett.*, 30, <https://doi.org/10.1029/2003GL017168>, 2003.
- Fraund, M., Pham, D., Bonanno, D., Harder, T., Wang, B., Brito, J., de Sá, S., Carbone, S., China, S., Artaxo, P., Martin, S., Pöhlker, C., Andreae, M., Laskin, A., Gilles, M., and Moffet, R.: Elemental Mixing State of Aerosol Particles Collected in Central Amazonia during GoAmazon2014/15, *Atmosphere*, 8, 173–201, <https://doi.org/10.3390/atmos8090173>, 2017.
- 670 Fraund, M., Park, T., Yao, L., Bonanno, D., Pham, D. Q., and Moffet, R. C.: Quantitative capabilities of STXM to measure spatially resolved organic volume fractions of mixed organic/inorganic particles, *Atmos. Meas. Tech.*, 12, 1619–1633, <https://doi.org/10.5194/amt-12-1619-2019>, 2019.
- 675 Froyd, K. D., Murphy, D. M., Brock, C. A., Campuzano-Jost, P., Dibb, J. E., Jimenez, J.-L., Kupc, A., Middlebrook, A. M., Schill, G. P., Thornhill, K. L., Williamson, C. J., Wilson, J. C., and Ziemba, L. D.: A new method to quantify mineral dust and other aerosol species from aircraft platforms using single-particle mass spectrometry, *Atmos. Meas. Tech.*, 12, 6209–6239, <https://doi.org/10.5194/amt-12-6209-2019>, 2019.
- Gonçalves, S. J., Weis, J., China, S., Evangelista, H., Harder, T. H., Müller, S., Sampaio, M., Laskin, A., Gilles, M. K., and Godoi, R. H. M.: Photochemical reactions on aerosols at West Antarctica: A molecular case-study of nitrate formation among sea salt aerosols, *Sci. Total Environ.*, 758, 143586, <https://doi.org/10.1016/j.scitotenv.2020.143586>, 2021.
- 680 Gunsch, M. J., Kirpes, R. M., Kolesar, K. R., Barrett, T. E., China, S., Sheesley, R. J., Laskin, A., Wiedensohler, A., Tuch, T., and Pratt, K. A.: Contributions of transported Prudhoe Bay oil field emissions to the aerosol population in Utqiagvik, Alaska, *Atmos. Chem. Phys.*, 17, 10879–10892, <https://doi.org/10.5194/acp-17-10879-2017>, 2017.
- Hamilton, D. S., Lee, L. A., Pringle, K. J., Reddington, C. L., Spracklen, D. V., and Carslaw, K. S.: Occurrence of pristine aerosol environments on a polluted planet, *Proc. Natl. Acad. Sci.*, 111, 18466–18471, <https://doi.org/10.1073/pnas.1415440111>, 2014.
- 685 Harwood, J. L. and Guschina, I. A.: The versatility of algae and their lipid metabolism, *Biochimie*, 91, 679–684, <https://doi.org/10.1016/j.biochi.2008.11.004>, 2009.
- Hems, R. F., Schnitzler, E. G., Liu-Kang, C., Cappa, C. D., and Abbatt, J. P. D.: Aging of Atmospheric Brown Carbon Aerosol, *ACS Earth Space Chem.*, 5, 722–748, <https://doi.org/10.1021/acsearthspacechem.0c00346>, 2021.
- 690 Hodshire, A. L., Campuzano-Jost, P., Kodros, J. K., Croft, B., Nault, B. A., Schroder, J. C., Jimenez, J. L., and Pierce, J. R.: The potential role of methanesulfonic acid (MSA) in aerosol formation and growth and the associated radiative forcings, *Atmos. Chem. Phys.*, 19, 3137–3160, <https://doi.org/10.5194/acp-19-3137-2019>, 2019.

- Holder, A. L., Gullett, B. K., Urbanski, S. P., Elleman, R., O'Neill, S., Tabor, D., Mitchell, W., and Baker, K. R.: Emissions from prescribed burning of agricultural fields in the Pacific Northwest, *Atmos. Environ.*, 166, 22–33, <https://doi.org/10.1016/j.atmosenv.2017.06.043>, 2017.
- 695 Holmes, N. S.: A review of particle formation events and growth in the atmosphere in the various environments and discussion of mechanistic implications, *Atmos. Environ.*, 41, 2183–2201, <https://doi.org/10.1016/j.atmosenv.2006.10.058>, 2007.
- Hopkins, R. J., Tivanski, A. V., Marten, B. D., and Gilles, M. K.: Chemical bonding and structure of black carbon reference materials and individual carbonaceous atmospheric aerosols, *J. Aerosol Sci.*, 38, 573–591, <https://doi.org/10.1016/j.jaerosci.2007.03.009>, 2007.
- 700 Igel, A. L., Ekman, A. M. L., Leck, C., Tjernström, M., Savre, J., and Sedlar, J.: The free troposphere as a potential source of arctic boundary layer aerosol particles: Free Troposphere and Boundary Layer Arctic Aerosol, *Geophys. Res. Lett.*, 44, 7053–7060, <https://doi.org/10.1002/2017GL073808>, 2017.
- Ilotoviz, E., Ghate, V. P., and Raveh-Rubin, S.: The Impact of Slantwise Descending Dry Intrusions on the Marine Boundary Layer and Air-Sea Interface Over the ARM Eastern North Atlantic Site, *J. Geophys. Res. Atmospheres*, 126, <https://doi.org/10.1029/2020JD033879>, 2021.
- 705 Jacobson, M. Z.: Strong radiative heating due to the mixing state of black carbon in atmospheric aerosols, *Nature*, 409, 695–697, <https://doi.org/10.1038/35055518>, 2001.
- Johnson, B. T., Shine, K. P., and Forster, P. M.: The semi-direct aerosol effect: Impact of absorbing aerosols on marine stratocumulus, *Q. J. R. Meteorol. Soc.*, 130, 1407–1422, <https://doi.org/10.1256/qj.03.61>, 2004.
- 710 Kawamura, Kimitaka. and Kaplan, I. R.: Motor exhaust emissions as a primary source for dicarboxylic acids in Los Angeles ambient air, *Environ. Sci. Technol.*, 21, 105–110, <https://doi.org/10.1021/es00155a014>, 1987.
- Khalizov, A. F., Lin, Y., Qiu, C., Guo, S., Collins, D., and Zhang, R.: Role of OH-Initiated Oxidation of Isoprene in Aging of Combustion Soot, *Environ. Sci. Technol.*, 47, 2254–2263, <https://doi.org/10.1021/es3045339>, 2013.
- 715 Kilcoyne, A. L. D., Tyliszczak, T., Steele, W. F., Fakra, S., Hitchcock, P., Franck, K., Anderson, E., Harteneck, B., Rightor, E. G., Mitchell, G. E., Hitchcock, A. P., Yang, L., Warwick, T., and Ade, H.: Interferometer-controlled scanning transmission X-ray microscopes at the Advanced Light Source, *J. Synchrotron Radiat.*, 10, 125–136, <https://doi.org/10.1107/S0909049502017739>, 2003.
- King, S. M., Butcher, A. C., Rosenoern, T., Coz, E., Lieke, K. I., de Leeuw, G., Nilsson, E. D., and Bilde, M.: Investigating Primary Marine Aerosol Properties: CCN Activity of Sea Salt and Mixed Inorganic–Organic Particles, *Environ. Sci. Technol.*, 46, 10405–10412, <https://doi.org/10.1021/es300574u>, 2012.
- 720 Klein, S. A., Zhang, Y., Zelinka, M. D., Pincus, R., Boyle, J., and Gleckler, P. J.: Are climate model simulations of clouds improving? An evaluation using the ISCCP simulator: Evaluating clouds in climate models, *J. Geophys. Res. Atmospheres*, 118, 1329–1342, <https://doi.org/10.1002/jgrd.50141>, 2013.
- 725 Kleinman, L. I., Springston, S. R., Daum, P. H., Weinstein-Lloyd, J., Alexander, M. L., Hubbe, J., Ortega, J., Canagaratna, M. R., and Jayne, J.: The time evolution of aerosol composition over the Mexico City plateau, *Atmos Chem Phys*, 1559–1575, <https://doi.org/10.5194/acp-8-1559-2008>, 2008.
- Kloss, C., Berthet, G., Sellitto, P., Ploeger, F., Bucci, S., Khaykin, S., Jégou, F., Taha, G., Thomason, L. W., Barret, B., Le Flochmoen, E., von Hobe, M., Bossolasco, A., Bègue, N., and Legras, B.: Transport of the 2017 Canadian wildfire plume to the tropics via the Asian monsoon circulation, *Atmos. Chem. Phys.*, 19, 13547–13567, <https://doi.org/10.5194/acp-19-13547-2019>, 2019.
- 730 Korhonen, H., Carslaw, K. S., Spracklen, D. V., Mann, G. W., and Woodhouse, M. T.: Influence of oceanic dimethyl sulfide emissions on cloud condensation nuclei concentrations and seasonality over the remote Southern Hemisphere oceans: A global model study, *J. Geophys. Res.*, 113, D15204, <https://doi.org/10.1029/2007JD009718>, 2008.

- Korolev, A. V., Emery, E. F., Strapp, J. W., Cober, S. G., Isaac, G. A., Wasey, M., and Marcotte, D.: Small Ice Particles in Tropospheric Clouds: Fact or Artifact? Airborne Icing Instrumentation Evaluation Experiment, *Bull. Am. Meteorol. Soc.*, 92, 967–973, <https://doi.org/10.1175/2010BAMS3141.1>, 2011.
- 735
- Kulkarni, P. and Wang, J.: New fast integrated mobility spectrometer for real-time measurement of aerosol size distribution—I: Concept and theory, *J. Aerosol Sci.*, 37, 1303–1325, <https://doi.org/10.1016/j.jaerosci.2006.01.005>, 2006.
- Kulmala, M., Pirjola, L., and Mäkelä, J. M.: Stable sulphate clusters as a source of new atmospheric particles, *Nature*, 404, 66–69, <https://doi.org/10.1038/35003550>, 2000.
- 740 Laskin, A., Iedema, M. J., and Cowin, J. P.: Time-Resolved Aerosol Collector for CCSEM/EDX Single-Particle Analysis, *Aerosol Sci. Technol.*, 37, 246–260, <https://doi.org/10.1080/02786820300945>, 2003.
- Laskin, A., Wietsma, T. W., Krueger, B. J., and Grassian, V. H.: Heterogeneous chemistry of individual mineral dust particles with nitric acid: A combined CCSEM/EDX, ESEM, and ICP-MS study, *J. Geophys. Res.*, 110, D10208 1-15, <https://doi.org/10.1029/2004JD005206>, 2005.
- 745 Laskin, A., Cowin, J. P., and Iedema, M. J.: Analysis of individual environmental particles using modern methods of electron microscopy and X-ray microanalysis, *J. Electron Spectrosc. Relat. Phenom.*, 150, 260–274, <https://doi.org/10.1016/j.elspec.2005.06.008>, 2006.
- Laskin, A., Moffet, R. C., Gilles, M. K., Fast, J. D., Zaveri, R. A., Wang, B., Nigge, P., and Shutthanandan, J.: Tropospheric chemistry of internally mixed sea salt and organic particles: Surprising reactivity of NaCl with weak organic acids: Mixed Sea Salt/Organics Particles, *J. Geophys. Res. Atmospheres*, 117, D15302 1-12, <https://doi.org/10.1029/2012JD017743>, 2012.
- 750 Laskin, A., Moffet, R. C., and Gilles, M. K.: Chemical Imaging of Atmospheric Particles, *Acc. Chem. Res.*, 52, 3419–3431, <https://doi.org/10.1021/acs.accounts.9b00396>, 2019.
- Lawrence, J. R., Swerhone, G. D. W., Leppard, G. G., Araki, T., Zhang, X., West, M. M., and Hitchcock, A. P.: Scanning Transmission X-Ray, Laser Scanning, and Transmission Electron Microscopy Mapping of the Exopolymeric Matrix of Microbial Biofilms, *Appl. Environ. Microbiol.*, 69, 5543–5554, <https://doi.org/10.1128/AEM.69.9.5543-5554.2003>, 2003.
- 755 Levin, E. J. T., McMeeking, G. R., Carrico, C. M., Mack, L. E., Kreidenweis, S. M., Wold, C. E., Moosmüller, H., Arnott, W. P., Hao, W. M., Collett, J. L., and Malm, W. C.: Biomass burning smoke aerosol properties measured during Fire Laboratory at Missoula Experiments (FLAME), *J. Geophys. Res.*, 115, D18210, <https://doi.org/10.1029/2009JD013601>, 2010.
- Levin, Z. and Cotton, W. R. (Eds.): *Aerosol pollution impact on precipitation: a scientific review*, Springer, Dordrecht ; London, 18–19 pp., 2009.
- 760 Li, J., Pósfai, M., Hobbs, P. V., and Buseck, P. R.: Individual aerosol particles from biomass burning in southern Africa: 2, Compositions and aging of inorganic particles: Composition and Aging of Inorganic Particles, *J. Geophys. Res. Atmospheres*, 108, 8484–8496, <https://doi.org/10.1029/2002JD002310>, 2003.
- 765 Li, W., Sun, J., Xu, L., Shi, Z., Riemer, N., Sun, Y., Fu, P., Zhang, J., Lin, Y., Wang, X., Shao, L., Chen, J., Zhang, X., Wang, Z., and Wang, W.: A conceptual framework for mixing structures in individual aerosol particles: Individual Aerosol Mixing Structure, *J. Geophys. Res. Atmospheres*, 121, 13,784-13,798, <https://doi.org/10.1002/2016JD025252>, 2016.
- Liu, X., Zhang, Y., Huey, L. G., Yokelson, R. J., Wang, Y., Jimenez, J. L., Campuzano-Jost, P., Beyersdorf, A. J., Blake, D. R., Choi, Y., St. Clair, J. M., Crouse, J. D., Day, D. A., Diskin, G. S., Fried, A., Hall, S. R., Hanisco, T. F., King, L. E., Meinardi, S., Mikoviny, T., Palm, B. B., Peischl, J., Perring, A. E., Pollack, I. B., Ryerson, T. B., Sachse, G., Schwarz, J. P., Simpson, I. J., Tanner, D. J., Thornhill, K. L., Ullmann, K., Weber, R. J., Wennberg, P. O., Wisthaler, A., Wolfe, G. M., and Ziemba, L. D.: Agricultural fires in the southeastern U.S. during SEAC⁴ RS: Emissions of trace gases and particles and evolution of ozone, reactive nitrogen, and organic aerosol: Agricultural Fires in the SE US, *J. Geophys. Res. Atmospheres*, 121, 7383–7414, <https://doi.org/10.1002/2016JD025040>, 2016.
- 770 Maria, S. F., Lynn, R. M., Gilles, M. K., and Myneni, S. C. B.: Organic Aerosol Growth Mechanisms and Their Climate-Forcing Implications, *Science*, 306, 1921–1924, <https://doi.org/10.1126/science.1103491>, 2004.
- 775

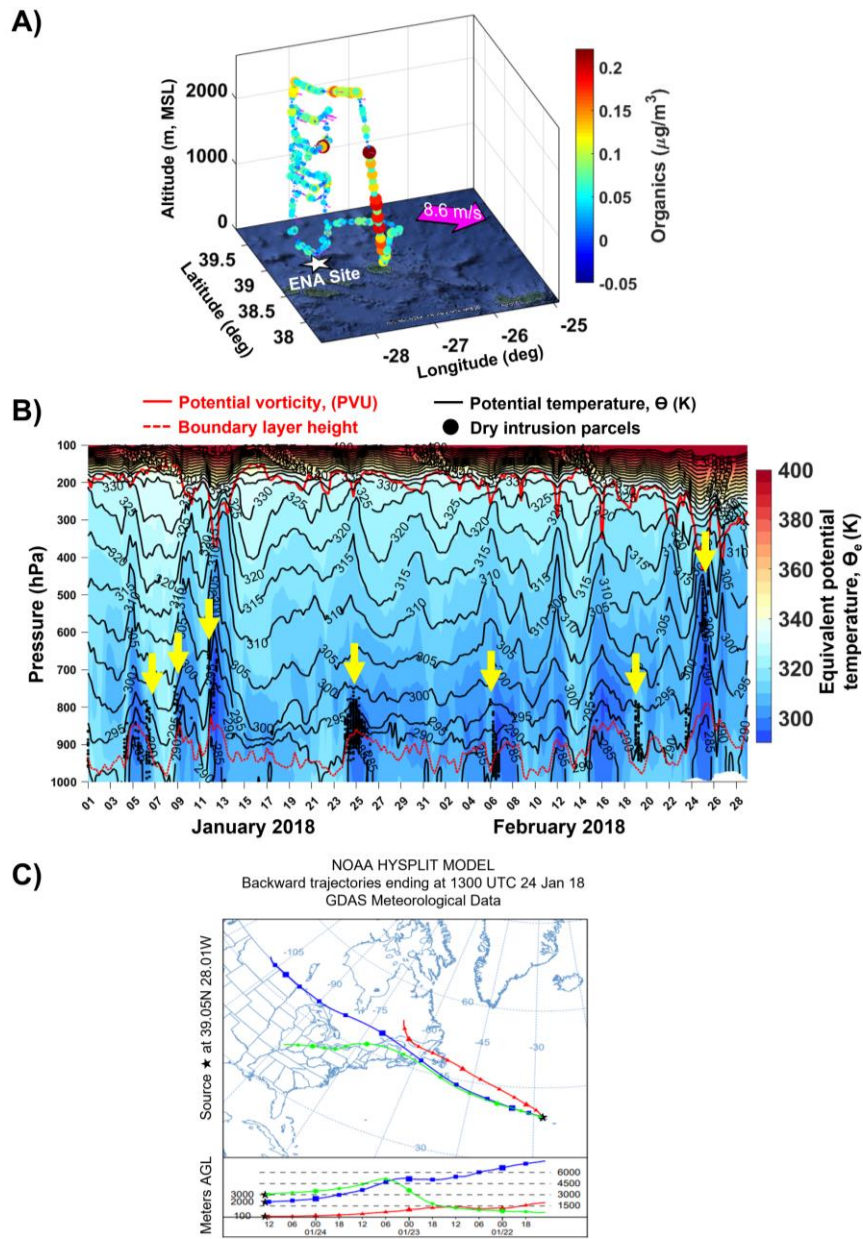
- Miyazaki, Y., Yamashita, Y., Kawana, K., Tachibana, E., Kagami, S., Mochida, M., Suzuki, K., and Nishioka, J.: Chemical transfer of dissolved organic matter from surface seawater to sea spray water-soluble organic aerosol in the marine atmosphere, *Sci. Rep.*, 8, 14861, <https://doi.org/10.1038/s41598-018-32864-7>, 2018.
- 780 Moffet, R. C., Henn, T., Laskin, A., and Gilles, M. K.: Automated Chemical Analysis of Internally Mixed Aerosol Particles Using X-ray Spectromicroscopy at the Carbon K-Edge, *Anal. Chem.*, 82, 7906–7914, <https://doi.org/10.1021/ac1012909>, 2010a.
- Moffet, R. C., Henn, T. R., Tivanski, A. V., Hopkins, R. J., Desyaterik, Y., Kilcoyne, A. L. D., Tylliszczak, T., Fast, J., Barnard, J., Shutthanandan, V., Cliff, S. S., Perry, K. D., Laskin, A., and Gilles, M. K.: Microscopic characterization of carbonaceous aerosol particle aging in the outflow from Mexico City, *Atmos Chem Phys*, 961–976, <https://doi.org/10.5194/acp-10-961-2010>, 2010b.
- 785 Moffet, R. C., Tivanski, A. V., and Gilles, M. K. (Eds.): Scanning Transmission X-ray Microscopy: Applications in Atmospheric Aerosol Research, in: *Fundamentals and Applications in Aerosol Spectroscopy*, Taylor and Francis Books, New York, 438–481, <https://doi.org/10.1201/b10417-21>, 2010c.
- Moffet, R. C., Furutani, H., Rödel, T. C., Henn, T. R., Sprau, P. O., Laskin, A., Uematsu, M., and Gilles, M. K.: Iron speciation and mixing in single aerosol particles from the Asian continental outflow: Aerosol Iron Speciation in Asian Outflow, *J. Geophys. Res. Atmospheres*, 117, D07204 1-12, <https://doi.org/10.1029/2011JD016746>, 2012.
- 790 Moffet, R. C., Rödel, T. C., Kelly, S. T., Yu, X. Y., Carroll, G. T., Fast, J., Zaveri, R. A., Laskin, A., and Gilles, M. K.: Spectromicroscopic measurements of carbonaceous aerosol aging in Central California, *Atmos. Chem. Phys.*, 13, 10445–10459, <https://doi.org/10.5194/acp-13-10445-2013>, 2013.
- Moffet, R. C., O'Brien, R. E., Alpert, P. A., Kelly, S. T., Pham, D. Q., Gilles, M. K., Knopf, D. A., and Laskin, A.: Morphology and mixing of black carbon particles collected in central California during the CARES field study, *Atmos. Chem. Phys.*, 16, 14515–14525, <https://doi.org/10.5194/acp-16-14515-2016>, 2016.
- 795 Mozurkewich, M.: Aerosol Growth and the Condensation Coefficient for Water: A Review, *Aerosol Sci. Technol.*, 5, 223–236, <https://doi.org/10.1080/02786828608959089>, 1986.
- Mungall, E. L., Abbatt, J. P. D., Wentzell, J. J. B., Lee, A. K. Y., Thomas, J. L., Blais, M., Gosselin, M., Miller, L. A., Papakyriakou, T., Willis, M. D., and Liggio, J.: Microlayer source of oxygenated volatile organic compounds in the summertime marine Arctic boundary layer, *Proc. Natl. Acad. Sci.*, 114, 6203–6208, <https://doi.org/10.1073/pnas.1620571114>, 2017.
- 800 Murphy, D. M. and Thomson, D. S.: Chemical composition of single aerosol particles at Idaho Hill: Negative ion measurements, *J. Geophys. Res. Atmospheres*, 102, 6353–6368, <https://doi.org/10.1029/96JD00859>, 1997.
- National Research Council (U.S.) (Ed.): The Congestion Mitigation and Air Quality Improvement Program: assessing 10 years of experience, Transportation Research Board, National Research Council : National Academy Press, Washington, D.C, 175–176 pp., 2002.
- 805 Nováková, E., Mitrea, G., Peth, C., Thieme, J., Mann, K., and Salditt, T.: Solid supported multicomponent lipid membranes studied by x-ray spectromicroscopy, *Biointerphases*, 3, FB44–FB54, <https://doi.org/10.1116/1.2976445>, 2008.
- O'Dowd, C. D., Facchini, M. C., Cavalli, F., Ceburnis, D., Mircea, M., Decesari, S., Fuzzi, S., Yoon, Y. J., and Putaud, J.-P.: Biogenically driven organic contribution to marine aerosol, *Nature*, 431, 676–680, <https://doi.org/10.1038/nature02959>, 2004.
- 810 Ovadnevaite, J., Zuend, A., Laaksonen, A., Sanchez, K. J., Roberts, G., Ceburnis, D., Decesari, S., Rinaldi, M., Hodas, N., Facchini, M. C., Seinfeld, J. H., and O' Dowd, C.: Surface tension prevails over solute effect in organic-influenced cloud droplet activation, *Nature*, 546, 637–641, <https://doi.org/10.1038/nature22806>, 2017.
- Owen, R. C., Cooper, O. R., Stohl, A., and Honrath, R. E.: An analysis of the mechanisms of North American pollutant transport to the central North Atlantic lower free troposphere, *J. Geophys. Res. Atmospheres*, 111, D23S58 1-14, <https://doi.org/10.1029/2006JD007062>, 2006.
- 815 Paredes-Miranda, G., Arnott, W. P., Moosmüller, H., Green, M. C., and Gyawali, M.: Black Carbon Aerosol Concentration in Five Cities and Its Scaling with City Population, *Bull. Am. Meteorol. Soc.*, 94, 41–50, <https://doi.org/10.1175/BAMS-D-11-00225.1>, 2013.

- 820 Park, R. J., Jacob, D. J., and Logan, J. A.: Fire and biofuel contributions to annual mean aerosol mass concentrations in the United States, *Atmos. Environ.*, 41, 7389–7400, <https://doi.org/10.1016/j.atmosenv.2007.05.061>, 2007.
- Petters, M. D. and Kreidenweis, S. M.: A single parameter representation of hygroscopic growth and cloud condensation nucleus activity, *Atmos Chem Phys*, 7, 1961–1971, <https://doi.org/10.5194/acp-7-1961-2007>, 2007.
- 825 Pham, D. Q., O'Brien, R., Fraund, M., Bonanno, D., Laskina, O., Beall, C., Moore, K. A., Forestieri, S., Wang, X., Lee, C., Sultana, C., Grassian, V., Cappa, C. D., Prather, K. A., and Moffet, R. C.: Biological Impacts on Carbon Speciation and Morphology of Sea Spray Aerosol, *ACS Earth Space Chem.*, 1, 551–561, <https://doi.org/10.1021/acsearthspacechem.7b00069>, 2017.
- Pincus, R. and Baker, M. B.: Effect of precipitation on the albedo susceptibility of clouds in the marine boundary layer, *Nature*, 372, 250–252, <https://doi.org/10.1038/372250a0>, 1994.
- Prather, K. A., Hatch, C. D., and Grassian, V. H.: Analysis of Atmospheric Aerosols, *Annu. Rev. Anal. Chem.*, 1, 485–514, <https://doi.org/10.1146/annurev.anchem.1.031207.113030>, 2008.
- 830 Prather, K. A., Bertram, T. H., Grassian, V. H., Deane, G. B., Stokes, M. D., DeMott, P. J., Aluwihare, L. I., Palenik, B. P., Azam, F., Seinfeld, J. H., Moffet, R. C., Molina, M. J., Cappa, C. D., Geiger, F. M., Roberts, G. C., Russell, L. M., Ault, A. P., Baltrusaitis, J., Collins, D. B., Corrigan, C. E., Cuadra-Rodriguez, L. A., Ebben, C. J., Forestieri, S. D., Guasco, T. L., Hersey, S. P., Kim, M. J., Lambert, W. F., Modini, R. L., Mui, W., Pedler, B. E., Ruppel, M. J., Ryder, O. S., Schoepp, N. G., Sullivan, R. C., and Zhao, D.: Bringing the ocean into the laboratory to probe the chemical complexity of sea spray aerosol, *Proc. Natl. Acad. Sci.*, 110, 7550–
835 7555, <https://doi.org/10.1073/pnas.1300262110>, 2013.
- Pratt, K. A. and Prather, K. A.: Aircraft measurements of vertical profiles of aerosol mixing states, *J. Geophys. Res.*, 115, D11305, <https://doi.org/10.1029/2009JD013150>, 2010.
- Raes, F.: Entrainment of free tropospheric aerosols as a regulating mechanism for cloud condensation nuclei in the remote marine boundary layer, *J. Geophys. Res.*, 100, 2893, <https://doi.org/10.1029/94JD02832>, 1995.
- 840 Ramnarine, E., Kodros, J. K., Hodshire, A. L., Lonsdale, C. R., Alvarado, M. J., and Pierce, J. R.: Effects of near-source coagulation of biomass burning aerosols on global predictions of aerosol size distributions and implications for aerosol radiative effects, *Atmos. Chem. Phys.*, 19, 6561–6577, <https://doi.org/10.5194/acp-19-6561-2019>, 2019.
- Raveh-Rubin, S.: Dry Intrusions: Lagrangian Climatology and Dynamical Impact on the Planetary Boundary Layer, *J. Clim.*, 30, 6661–6682, <https://doi.org/10.1175/JCLI-D-16-0782.1>, 2017.
- 845 Raveh-Rubin, S. and Catto, J. L.: Climatology and dynamics of the link between dry intrusions and cold fronts during winter, Part II: Front-centred perspective, *Clim. Dyn.*, 53, 1893–1909, <https://doi.org/10.1007/s00382-019-04793-2>, 2019.
- Rebotier, T. P. and Prather, K. A.: Aerosol time-of-flight mass spectrometry data analysis: A benchmark of clustering algorithms, *Anal. Chim. Acta*, 585, 38–54, <https://doi.org/10.1016/j.aca.2006.12.009>, 2007.
- 850 Reddington, C. L., Carslaw, K. S., Spracklen, D. V., Frontoso, M. G., Collins, L., Merikanto, J., Minikin, A., Hamburger, T., Coe, H., Kulmala, M., Aalto, P., Flentje, H., Plass-Dülmer, C., Birmili, W., Wiedensohler, A., Wehner, B., Tuch, T., Sonntag, A., O'Dowd, C. D., Jennings, S. G., Dupuy, R., Baltensperger, U., Weingartner, E., Hansson, H.-C., Tunved, P., Laj, P., Sellegri, K., Boulon, J., Putaud, J.-P., Gruening, C., Swietlicki, E., Roldin, P., Henzing, J. S., Moerman, M., Mihalopoulos, N., Kouvarakis, G., Ždímal, V., Žíková, N., Marinoni, A., Bonasoni, P., and Duchi, R.: Primary versus secondary contributions to particle number
855 concentrations in the European boundary layer, *Atmos. Chem. Phys.*, 11, 12007–12036, <https://doi.org/10.5194/acp-11-12007-2011>, 2011.
- Reff, A., Bhave, P. V., Simon, H., Pace, T. G., Pouliot, G. A., Mobley, J. D., and Houyoux, M.: Emissions Inventory of PM_{2.5} Trace Elements across the United States, *Environ. Sci. Technol.*, 43, 5790–5796, <https://doi.org/10.1021/es802930x>, 2009.
- Ren, J., Zhang, F., Wang, Y., Collins, D., Fan, X., Jin, X., Xu, W., Sun, Y., Cribb, M., and Li, Z.: Using different assumptions of aerosol mixing state and chemical composition to predict CCN concentrations based on field measurements in urban Beijing,
860 *Atmos. Chem. Phys.*, 18, 6907–6921, <https://doi.org/10.5194/acp-18-6907-2018>, 2018.
- Riemer, N., Ault, A. P., West, M., Craig, R. L., and Curtis, J. H.: Aerosol Mixing State: Measurements, Modeling, and Impacts, *Rev. Geophys.*, 57, 187–249, <https://doi.org/10.1029/2018RG000615>, 2019.

- 865 Roberts, G. C., Day, D. A., Russell, L. M., Dunlea, E. J., Jimenez, J. L., Tomlinson, J. M., Collins, D. R., Shinozuka, Y., and Clarke, A. D.: Characterization of particle cloud droplet activity and composition in the free troposphere and the boundary layer during INTEX-B, *Atmos. Chem. Phys.*, 10, 6627–6644, <https://doi.org/10.5194/acp-10-6627-2010>, 2010.
- Rolph, G., Stein, A., and Stunder, B.: Real-time Environmental Applications and Display sYstem: READY, *Environ. Model. Softw.*, 95, 210–228, <https://doi.org/10.1016/j.envsoft.2017.06.025>, 2017.
- Rosenfeld, D., Zhu, Y., Wang, M., Zheng, Y., Goren, T., and Yu, S.: Aerosol-driven droplet concentrations dominate coverage and water of oceanic low-level clouds, *Science*, 363, eaav0566, <https://doi.org/10.1126/science.aav0566>, 2019.
- 870 Ruehl, C. R., Davies, J. F., and Wilson, K. R.: An interfacial mechanism for cloud droplet formation on organic aerosols, *Science*, 351, 1447–1450, <https://doi.org/10.1126/science.aad4889>, 2016.
- Sanchez, K. J., Chen, C.-L., Russell, L. M., Betha, R., Liu, J., Price, D. J., Massoli, P., Ziemba, L. D., Crosbie, E. C., Moore, R. H., Müller, M., Schiller, S. A., Wisthaler, A., Lee, A. K. Y., Quinn, P. K., Bates, T. S., Porter, J., Bell, T. G., Saltzman, E. S., Vaillancourt, R. D., and Behrenfeld, M. J.: Substantial Seasonal Contribution of Observed Biogenic Sulfate Particles to Cloud Condensation Nuclei, *Sci. Rep.*, 8, 3235, <https://doi.org/10.1038/s41598-018-21590-9>, 2018.
- Schill, S. R., Collins, D. B., Lee, C., Morris, H. S., Novak, G. A., Prather, K. A., Quinn, P. K., Sultana, C. M., Tivanski, A. V., Zimmermann, K., Cappa, C. D., and Bertram, T. H.: The Impact of Aerosol Particle Mixing State on the Hygroscopicity of Sea Spray Aerosol, *ACS Cent. Sci.*, 1, 132–141, <https://doi.org/10.1021/acscentsci.5b00174>, 2015.
- Schmale, J., Henning, S., Henzing, B., Keskinen, H., Sellegri, K., Ovadnevaite, J., Bougiatioti, A., Kalivitis, N., Stavroulas, I., Jefferson, A., Park, M., Schlag, P., Kristensson, A., Iwamoto, Y., Pringle, K., Reddington, C., Aalto, P., Äijälä, M., Baltensperger, U., Bialek, J., Birmili, W., Bukowiecki, N., Ehn, M., Fjæraa, A. M., Fiebig, M., Frank, G., Fröhlich, R., Frumau, A., Furuya, M., Hammer, E., Heikkinen, L., Herrmann, E., Holzinger, R., Hyono, H., Kanakidou, M., Kiendler-Scharr, A., Kinouchi, K., Kos, G., Kulmala, M., Mihalopoulos, N., Motos, G., Nenes, A., O'Dowd, C., Paramonov, M., Petäjä, T., Picard, D., Poulain, L., Prévôt, A. S. H., Slowik, J., Sonntag, A., Swietlicki, E., Svenningsson, B., Tsurumaru, H., Wiedensohler, A., Wittbom, C., Ogren, J. A., 885 Matsuki, A., Yum, S. S., Myhre, C. L., Carslaw, K., Stratmann, F., and Gysel, M.: Collocated observations of cloud condensation nuclei, particle size distributions, and chemical composition, *Sci. Data*, 4, 170003, <https://doi.org/10.1038/sdata.2017.3>, 2017.
- Schmale, J., Henning, S., Decesari, S., Henzing, B., Keskinen, H., Sellegri, K., Ovadnevaite, J., Pöhlker, M. L., Brito, J., Bougiatioti, A., Kristensson, A., Kalivitis, N., Stavroulas, I., Carbone, S., Jefferson, A., Park, M., Schlag, P., Iwamoto, Y., Aalto, P., Äijälä, M., Bukowiecki, N., Ehn, M., Frank, G., Fröhlich, R., Frumau, A., Herrmann, E., Herrmann, H., Holzinger, R., Kos, G., 890 Kulmala, M., Mihalopoulos, N., Nenes, A., O'Dowd, C., Petäjä, T., Picard, D., Pöhlker, C., Pöschl, U., Poulain, L., Prévôt, A. S. H., Swietlicki, E., Andreae, M. O., Artaxo, P., Wiedensohler, A., Ogren, J., Matsuki, A., Yum, S. S., Stratmann, F., Baltensperger, U., and Gysel, M.: Long-term cloud condensation nuclei number concentration, particle number size distribution and chemical composition measurements at regionally representative observatories, *Atmos. Chem. Phys.*, 18, 2853–2881, <https://doi.org/10.5194/acp-18-2853-2018>, 2018.
- 895 Souri, A. H., Choi, Y., Jeon, W., Kochanski, A. K., Diao, L., Mandel, J., Bhave, P. V., and Pan, S.: Quantifying the Impact of Biomass Burning Emissions on Major Inorganic Aerosols and Their Precursors in the U.S.: Burning Impact on Inorganic Aerosols, *J. Geophys. Res. Atmospheres*, 122, 12,020–12,041, <https://doi.org/10.1002/2017JD026788>, 2017.
- Sprenger, M. and Wernli, H.: The LAGRANTO Lagrangian analysis tool – version 2.0, *Geosci. Model Dev.*, 8, 2569–2586, <https://doi.org/10.5194/gmd-8-2569-2015>, 2015.
- 900 Stein, A. F., Draxler, R. R., Rolph, G. D., Stunder, B. J. B., Cohen, M. D., and Ngan, F.: NOAA's HYSPLIT Atmospheric Transport and Dispersion Modeling System, *Bull. Am. Meteorol. Soc.*, 96, 2059–2077, <https://doi.org/10.1175/BAMS-D-14-00110.1>, 2015.
- Stull, R. B.: Mean Boundary Layer Characteristics, in: *An Introduction to Boundary Layer Meteorology*, Springer Netherlands, Dordrecht, 1–27, https://doi.org/10.1007/978-94-009-3027-8_1, 1988.
- Tomlin, J. M., Jankowski, K. A., Rivera-Adorno, F. A., Fraund, M., China, S., Stirn, B. H., Kaeser, R., Eakins, G. S., Moffet, R. C., Shepson, P. B., and Laskin, A.: Chemical Imaging of Fine Mode Atmospheric Particles Collected from a Research Aircraft over Agricultural Fields, *ACS Earth Space Chem.*, 4, 2171–2184, <https://doi.org/10.1021/acsearthspacechem.0c00172>, 2020.
- Toner, S. M., Sodeman, D. A., and Prather, K. A.: Single Particle Characterization of Ultrafine and Accumulation Mode Particles from Heavy Duty Diesel Vehicles Using Aerosol Time-of-Flight Mass Spectrometry, *Environ. Sci. Technol.*, 40, 3912–3921, <https://doi.org/10.1021/es051455x>, 2006.

- 910 Vakkari, V., Beukes, J. P., Dal Maso, M., Aurela, M., Josipovic, M., and van Zyl, P. G.: Major secondary aerosol formation in southern African open biomass burning plumes, *Nat. Geosci.*, 11, 580–583, <https://doi.org/10.1038/s41561-018-0170-0>, 2018.
- Val Martín, M., Honrath, R. E., Owen, R. C., Pfister, G., Fialho, P., and Barata, F.: Significant enhancements of nitrogen oxides, black carbon, and ozone in the North Atlantic lower free troposphere resulting from North American boreal wildfires, *J. Geophys. Res. Atmospheres*, 111, D23S60 1-17, <https://doi.org/10.1029/2006JD007530>, 2006.
- 915 VanReken, T. M.: Toward aerosol/cloud condensation nuclei (CCN) closure during CRYSTAL-FACE, *J. Geophys. Res.*, 108, 4633, <https://doi.org/10.1029/2003JD003582>, 2003.
- Wang, B., Lambe, A. T., Massoli, P., Onasch, T. B., Davidovits, P., Worsnop, D. R., and Knopf, D. A.: The deposition ice nucleation and immersion freezing potential of amorphous secondary organic aerosol: Pathways for ice and mixed-phase cloud formation, *J. Geophys. Res. Atmospheres*, 117, 1–12, <https://doi.org/10.1029/2012JD018063>, 2012.
- 920 Wang, B., Gilles, M. K., and Laskin, A.: Reactivity of Liquid and Semisolid Secondary Organic Carbon with Chloride and Nitrate in Atmospheric Aerosols, *J Phys Chem A*, 119, 4498–4508, <https://doi.org/doi.org/10.1021/jp510336q>, 2015a.
- Wang, J., Lee, Y.-N., Daum, P. H., Jayne, J., and Alexander, M. L.: Effects of aerosol organics on cloud condensation nucleus (CCN) concentration and first indirect aerosol effect, *Atmos Chem Phys*, 6325–6339, <https://doi.org/10.5194/acp-8-6325-2008>, 2008.
- 925 Wang, J., Cubison, M. J., Aiken, A. C., Jimenez, J. L., and Collins, D. R.: The importance of aerosol mixing state and size-resolved composition on CCN concentration and the variation of the importance with atmospheric aging of aerosols, *Atmos. Chem. Phys.*, 10, 7267–7283, <https://doi.org/10.5194/acp-10-7267-2010>, 2010.
- Wang, J., Wood, R., Jensen, M., Jui-Yuan Chiu, C., Liu, Y., Lamer, K., Desai, N., Giangrande, S., Knopf, D., Kollias, P., Laskin, A., Liu, X., Lu, C., Mechem, D., Mei, F., Starzec, M., Tomlinson, J., Wang, Y., Soo Yum, S., Zheng, G., Aiken, A., Eduardo, E. B., Blanchard, Y., China, S., Dong, X., Gallo, F., Gao, S., Ghate, V., Glienke, S., Hardin, J., Hubbe, J., Isom, B., Luke, E., Matthews, A. A., Miller, M. A., Moffet, R., Pekour, M., Schmid, B., Sedlacek, A. J., Shaw, R., Shilling, J., Springston, S., Sullivan, A., Suski, K., Veghte, D. P., Weber, R., Yeom, J., Wyant, M., Zawadowicz, M., and Zhang, Z.: Aerosol and Cloud Experiments in the Eastern North Atlantic (ACE-ENA), *Bull. Am. Meteorol. Soc.*, Revised version submitted, 2021a.
- 930 Wang, X., Sultana, C. M., Trueblood, J., Hill, T. C. J., Malfatti, F., Lee, C., Laskina, O., Moore, K. A., Beall, C. M., McCluskey, C. S., Cornwell, G. C., Zhou, Y., Cox, J. L., Pendergraft, M. A., Santander, M. V., Bertram, T. H., Cappa, C. D., Azam, F., DeMott, P. J., Grassian, V. H., and Prather, K. A.: Microbial Control of Sea Spray Aerosol Composition: A Tale of Two Blooms, *ACS Cent. Sci.*, 1, 124–131, <https://doi.org/10.1021/acscentsci.5b00148>, 2015b.
- Wang, Y., Pinterich, T., and Wang, J.: Rapid measurement of sub-micrometer aerosol size distribution using a fast integrated mobility spectrometer, *J. Aerosol Sci.*, 121, 12–20, <https://doi.org/10.1016/j.jaerosci.2018.03.006>, 2018.
- 940 Wang, Y., Zheng, X., Dong, X., Xi, B., Wu, P., Logan, T., and Yung, Y. L.: Impacts of long-range transport of aerosols on marine-boundary-layer clouds in the eastern North Atlantic, *Atmos. Chem. Phys.*, 20, 14741–14755, <https://doi.org/10.5194/acp-20-14741-2020>, 2020.
- Wang, Y., Zheng, G., Jensen, M., Knopf, D., Laskin, A., Matthews, A., Mechem, D., Mei, F., Moffet, R., Sedlacek, A., Shilling, J., Springston, S., Sullivan, A., Tomlinson, J., Veghte, D., Weber, R., Wood, R., Zawadowicz, M., and Wang, J.: Vertical profiles of trace gas and aerosol properties over the Eastern North Atlantic: Variations with season and synoptic condition, *Aerosols/Field Measurements/Troposphere/Physics (physical properties and processes)*, <https://doi.org/10.5194/acp-2021-300>, 2021b.
- 945 Wernli, H.: A Lagrangian-based analysis of extratropical cyclones. II: A detailed case-study, *Q. J. R. Meteorol. Soc.*, 123, 1677–1706, <https://doi.org/10.1002/qj.49712354211>, 1997.
- Willis, M. D., Köllner, F., Burkart, J., Bozem, H., Thomas, J. L., Schneider, J., Aliabadi, A. A., Hoor, P. M., Schulz, H., Herber, A. B., Leaitch, W. R., and Abbatt, J. P. D.: Evidence for marine biogenic influence on summertime Arctic aerosol, *Geophys. Res. Lett.*, 44, 6460–6470, <https://doi.org/10.1002/2017GL073359>, 2017.
- 950 Wood, R.: Stratocumulus Clouds, *Mon. Weather Rev.*, 140, 2373–2423, <https://doi.org/10.1175/MWR-D-11-00121.1>, 2012.

- Wood, R., Wyant, M., Bretherton, C. S., Rémillard, J., Kollias, P., Fletcher, J., Stemmler, J., de Szoeko, S., Yuter, S., Miller, M., Mechem, D., Tselioudis, G., Chiu, J. C., Mann, J. A. L., O'Connor, E. J., Hogan, R. J., Dong, X., Miller, M., Ghate, V., Jefferson, A., Min, Q., Minnis, P., Palikonda, R., Albrecht, B., Luke, E., Hannay, C., and Lin, Y.: Clouds, Aerosols, and Precipitation in the Marine Boundary Layer: An Arm Mobile Facility Deployment, *Bull. Am. Meteorol. Soc.*, 96, 419–440, <https://doi.org/10.1175/BAMS-D-13-00180.1>, 2015.
- Worsnop, D. R., Morris, J. W., Shi, Q., Davidovits, P., and Kolb, C. E.: A chemical kinetic model for reactive transformations of aerosol particles: Reactive transformation of aerosol particles, *Geophys. Res. Lett.*, 29, 57-1-57-4, <https://doi.org/10.1029/2002GL015542>, 2002.
- Yamasoe, M. A., Artaxo, P., Miguel, A. H., and Allen, A. G.: Chemical composition of aerosol particles from direct emissions of vegetation fires in the Amazon Basin: water-soluble species and trace elements, *Atmos. Environ.*, 34, 1641–1653, [https://doi.org/10.1016/S1352-2310\(99\)00329-5](https://doi.org/10.1016/S1352-2310(99)00329-5), 2000.
- Yu, P., Toon, O. B., Bardeen, C. G., Zhu, Y., Rosenlof, K. H., Portmann, R. W., Thornberry, T. D., Gao, R.-S., Davis, S. M., Wolf, E. T., de Gouw, J., Peterson, D. A., Fromm, M. D., and Robock, A.: Black carbon lofts wildfire smoke high into the stratosphere to form a persistent plume, *Science*, 365, 587–590, <https://doi.org/10.1126/science.aax1748>, 2019.
- Zawadowicz, M. A., Suski, K., Liu, J., Pekour, M., Fast, J., Mei, F., Sedlacek, A. J., Springston, S., Wang, Y., Zaveri, R. A., Wood, R., Wang, J., and Shilling, J. E.: Aircraft measurements of aerosol and trace gas chemistry in the eastern North Atlantic, *Atmos. Chem. Phys.*, 21, 7983–8002, <https://doi.org/10.5194/acp-21-7983-2021>, 2021.
- Zehr, J. P. and Ward, B. B.: Nitrogen Cycling in the Ocean: New Perspectives on Processes and Paradigms, *Appl. Environ. Microbiol.*, 68, 1015–1024, <https://doi.org/10.1128/AEM.68.3.1015-1024.2002>, 2002.
- Zheng, G., Wang, Y., Aiken, A. C., Gallo, F., Jensen, M. P., Kollias, P., Kuang, C., Luke, E., Springston, S., Uin, J., Wood, R., Wang, J., and Wang, J.: Marine boundary layer aerosol in the eastern North Atlantic: seasonal variations and key controlling processes, *Atmos Chem Phys*, 18, 17615–17635, <https://doi.org/10.5194/acp-18-17615-2018>, 2018.
- Zheng, G., Kuang, C., Uin, J., Watson, T., and Wang, J.: Large contribution of organics to condensational growth and formation of cloud condensation nuclei (CCN) in the remote marine boundary layer, *Atmos. Chem. Phys.*, 20, 12515–12525, <https://doi.org/10.5194/acp-20-12515-2020>, 2020a.
- Zheng, G., Sedlacek, A. J., Aiken, A. C., Feng, Y., Watson, T. B., Raveh-Rubin, S., Uin, J., Lewis, E. R., and Wang, J.: Long-range transported North American wildfire aerosols observed in marine boundary layer of eastern North Atlantic, *Environ. Int.*, 139, 105680, <https://doi.org/10.1016/j.envint.2020.105680>, 2020b.
- Zheng, G., Wang, Y., Wood, R., Jensen, M. P., Kuang, C., McCoy, I. L., Matthews, A., Mei, F., Tomlinson, J. M., Shilling, J. E., Zawadowicz, M. A., Crosbie, E., Moore, R., Ziemba, L., Andreae, M. O., and Wang, J.: New particle formation in the remote marine boundary layer, *Nat. Commun.*, 12, 527, <https://doi.org/10.1038/s41467-020-20773-1>, 2021.
- Zhou, S., Collier, S., Jaffe, D. A., and Zhang, Q.: Free tropospheric aerosols at the Mt. Bachelor Observatory: more oxidized and higher sulfate content compared to boundary layer aerosols, *Atmos. Chem. Phys.*, 19, 1571–1585, <https://doi.org/10.5194/acp-19-1571-2019>, 2019.
- Zhu, L., Val Martin, M., Gatti, L. V., Kahn, R., Hecobian, A., and Fischer, E. V.: Development and implementation of a new biomass burning emissions injection height scheme (BBEIH v1.0) for the GEOS-Chem model (v9-01-01), *Geosci. Model Dev.*, 11, 4103–4116, <https://doi.org/10.5194/gmd-11-4103-2018>, 2018.
- Zieger, P., Väisänen, O., Corbin, J. C., Partridge, D. G., Bastelberger, S., Mousavi-Fard, M., Rosati, B., Gysel, M., Krieger, U. K., Leck, C., Nenes, A., Riipinen, I., Virtanen, A., and Salter, M. E.: Revising the hygroscopicity of inorganic sea salt particles, *Nat. Commun.*, 8, 15883, <https://doi.org/10.1038/ncomms15883>, 2017.



995 **Figure 1.** A) A representative flight path of G-1 aircraft during one of the DI events (2018-01-24) during ACE-ENA campaign (Azores, Portugal). Size and color scale correspond to organic concentration provided by onboard Aerodyne HR-ToF-AMS. B) A time-height cross section at 39°N,28°W using ERA Interim reanalysis of ECMWF, showing equivalent potential temperature (K, shading), potential temperature (black contours) and boundary-layer height (red dashed line). The solid red line is the 2-PVU contour of potential vorticity, marking the tropopause. The time periods of DI events (marked by black dots and indicated by yellow arrows) were identified from calculated forward trajectories based on the wind field data (ERA Interim, see text for more details). C) Calculated HYSPLIT 72 hrs back trajectory for 2018-01-24 utilizing GDAS1 archived data sets starting at three elevations: 100 m (red), 2000 m (blue), 3000 m (green).

1005

1010

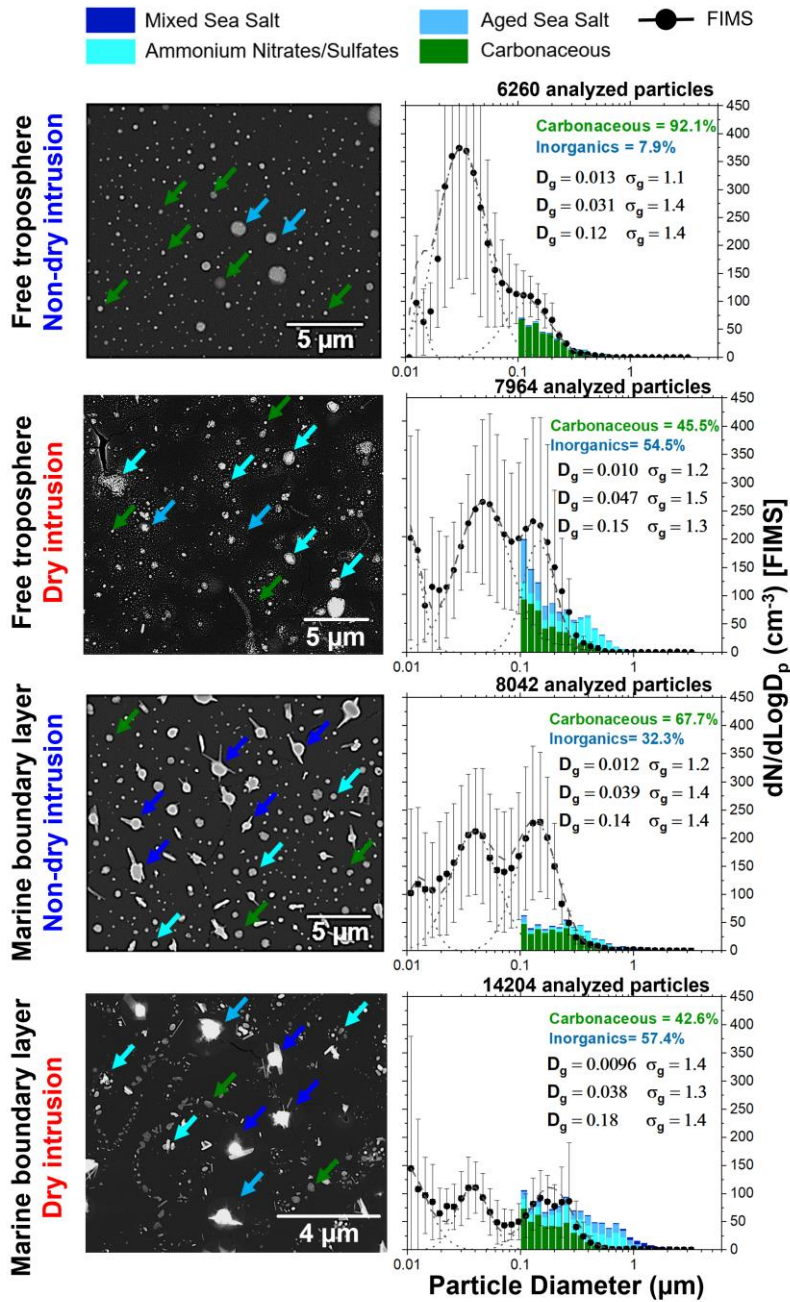
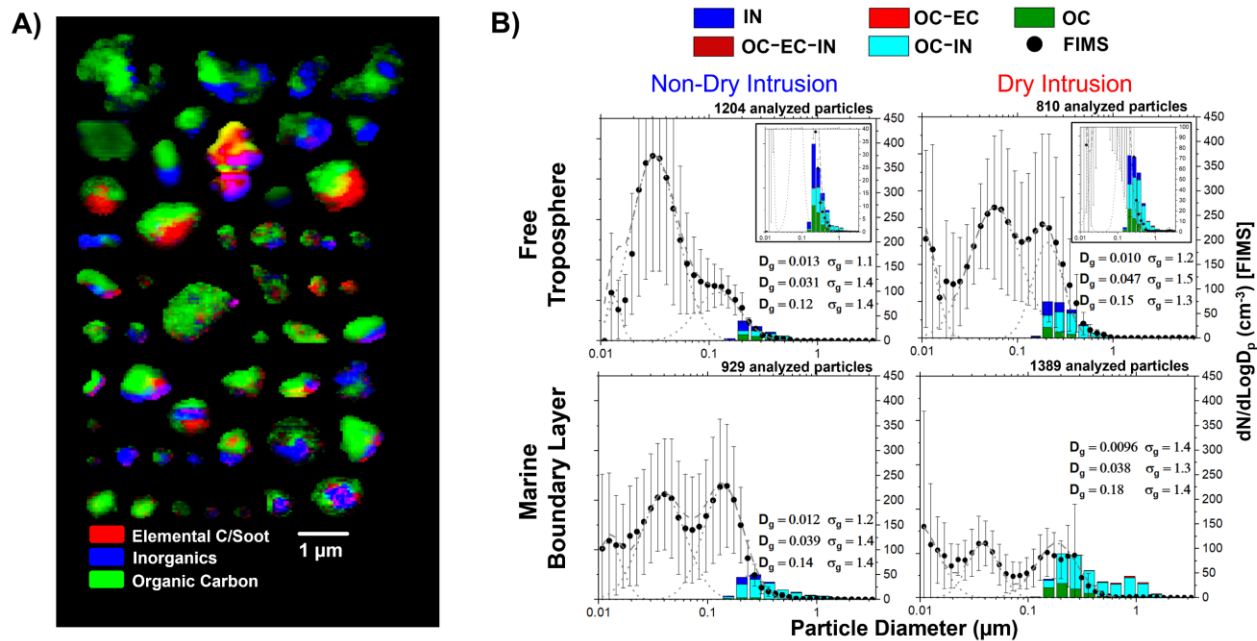


Figure 2. Representative backscattering mode SEM imaging of particles (left column) and relative particle-type populations (right column) determined by CCSEM/EDX and *k*-means clustering analysis, summarized as a 16 bin/decade histogram representative of MBL and FT atmospheric layers and DI versus non-DI synoptic conditions. The composition of the size-segregated particle-type population were broken down into “Carbonaceous” and “Inorganics” (i.e., Mixed Sea Salt + Aged Sea Salt + Ammonium Nitrate/Sulfate). The average FIMS aerosol size distribution measured onboard G1 is superimposed and anchored at 0.25 μm to facilitate a visual assessment of particle types and number concentrations for CCN active particles (>100 nm). Lognormal mode diameter (D_g) and standard deviation (σ_g) were fitted for the FIMS particle size distribution (grey dashed lines).

1015

1020

1025



1030 Figure 3. A) Carbon speciation map of a subset of particles acquired by STXM from DI periods. Note that components can overlap
 where each pixel can contain different combination of the individual components: EC + IN constituents as purple; OC + EC as yellow;
 OC + IN as cyan. B) Size distribution of analyzed particles identified via STXM/NEXAFS shown as an 8 bin/decade histogram to compare
 1035 particle multi-component internal mixing state between atmospheric transport events. FIMS particle size distribution is overlaid to
 facilitate a visual comparison from the same atmospheric episodes. Shown legends are as follows: IN–inorganics, OC–organic carbon
 (i.e., COOH), EC–elemental carbon (i.e., sp² C=C carbon).

1040

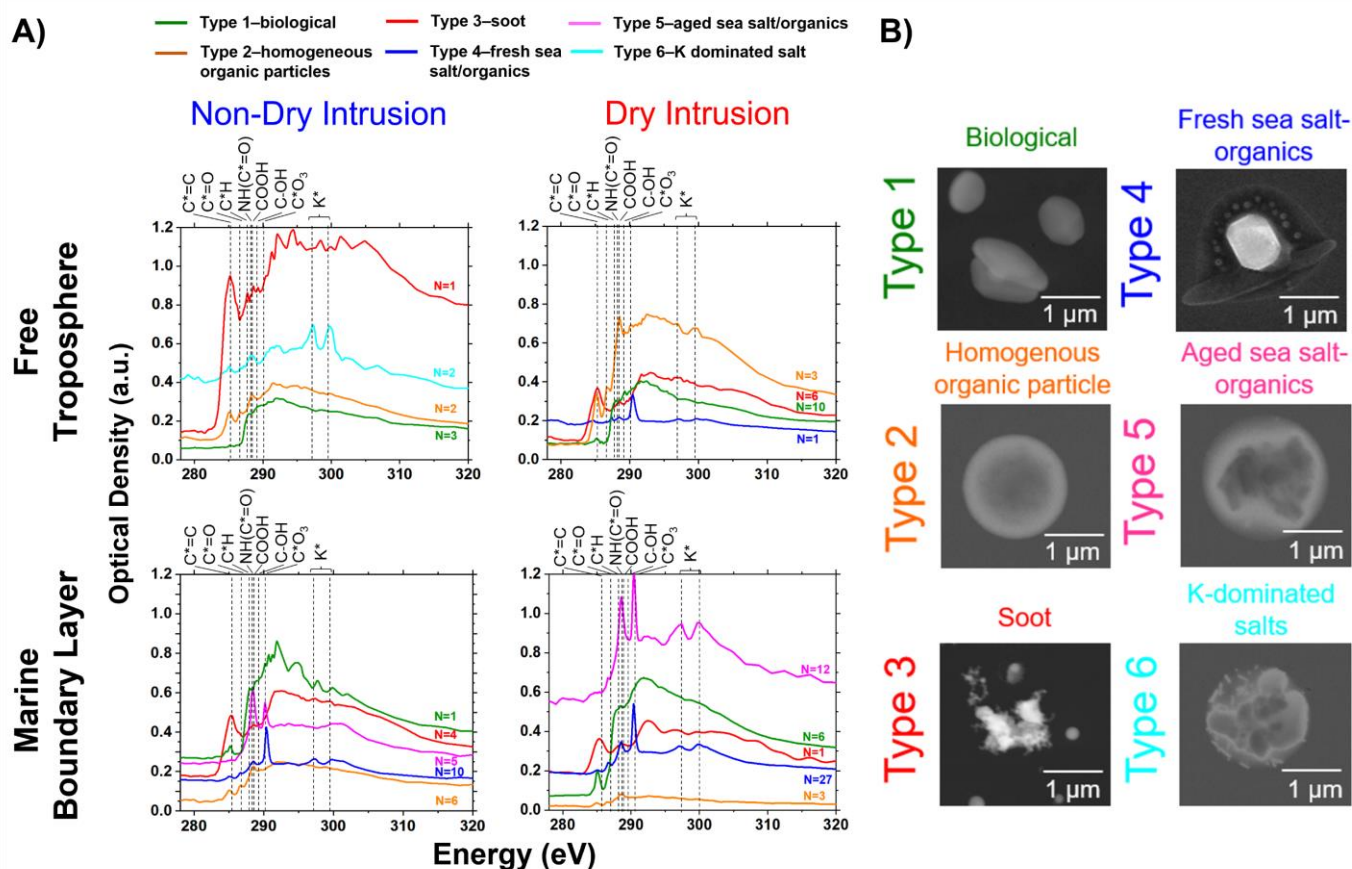


Figure 4. A) Individual NEXAFS spectra showing differences in carbon content of representative particles collected at MBL and FT altitudes under different synoptic conditions. Identified Carbon types are: “Type 1–biological” (green), “Type 2–homogeneous organic particles” (orange), “Type 3–soot” (red), “Type 4–fresh sea salt/organics” (blue), “Type 5–aged sea salt/organics” (pink), “Type 6–K dominated salt” (teal). Dashed lines correspond to the transition energies: 285.4 eV (C*=C), 286.7 eV (C*=O), 287.7 eV (C*-H), 288.3 eV (R-NH(C*=O)R), 288.5 eV (R(C*=O)OH), 289.5 eV (RC*-OH), 290.0 eV (C edge step), 290.4 eV (C*O₃), 297.1 eV (K*_{L2}), and 299.7 eV (K*_{L3}). B) Representative secondary electron mode SEM imaging of particles corresponding to the different carbon types identified with the STXM/NEXAFS analysis.

1045

1050

1055

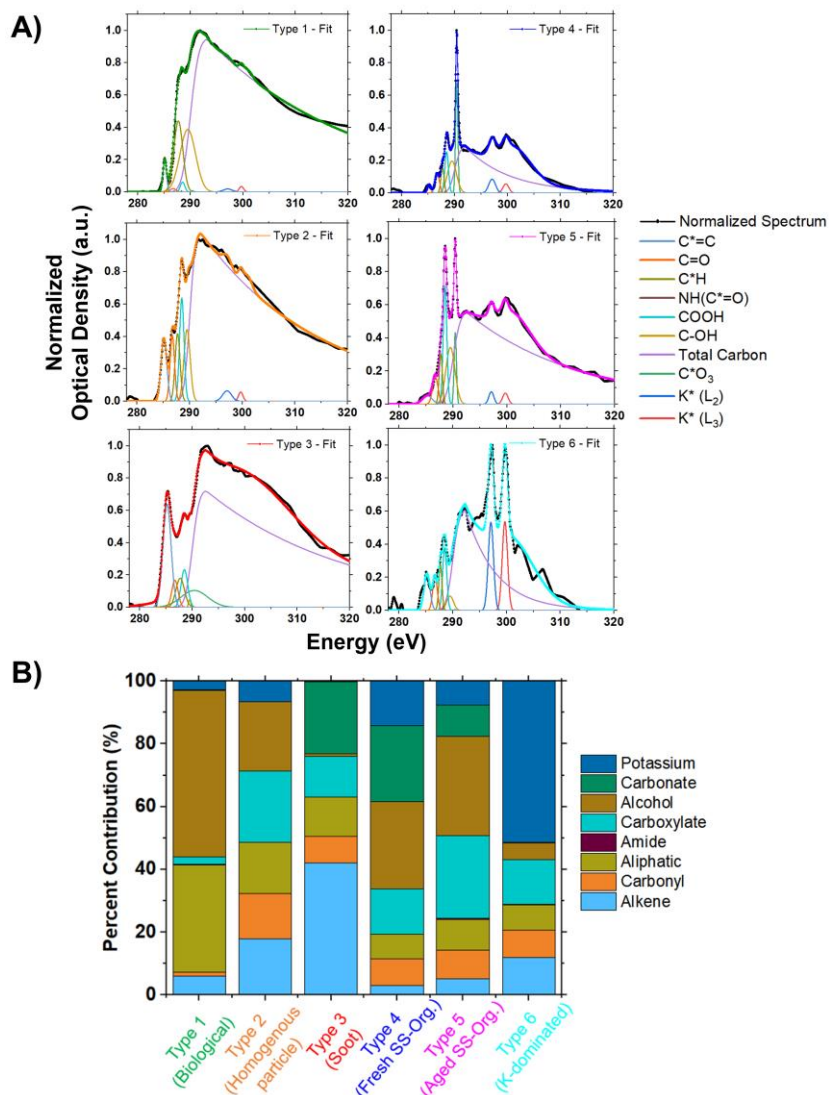


Figure 5. A) Carbon K-edge NEXAFS spectra of 6 carbon types identified in individual particles: “Type 1 – biological” (green), “Type 2 – homogeneous organic particles” (orange), “Type 3 – soot” (red), “Type 4 – fresh sea salt/organics” (blue), “Type 5 – aged sea salt/organics” (pink), “Type 6 – K dominated salt” (teal). B) Contributions of the different carbon functional groups reported as a percentage of the total peak area.

1060

1065

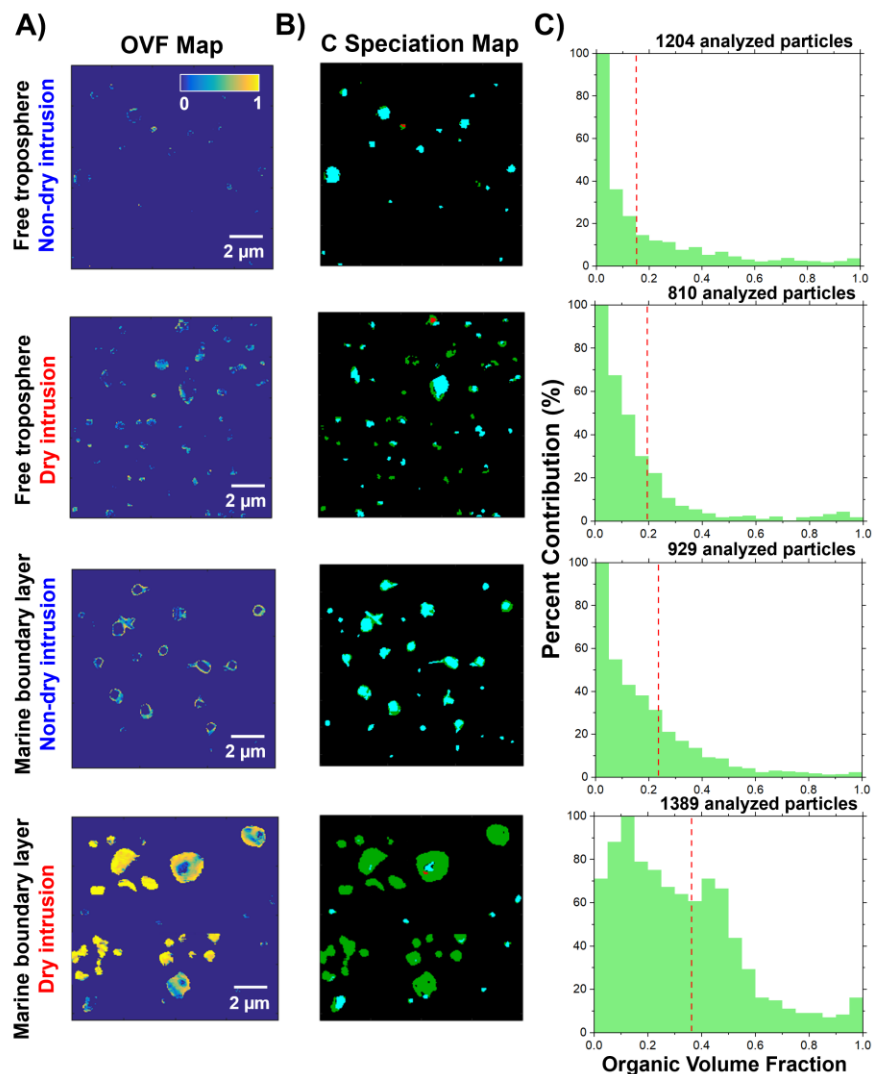


Figure 6. A) Representative organic volume fraction (OVF) maps of individual particles. B) Carbon speciation maps of the identical particles; Teal – inorganic dominant regions; Green – organic dominant regions (i.e., COOH); Red – elemental carbon (i.e., sp^2 carbon). C) Histogram of particle fractions as a function of their OVF values with average OVF (red dashed line). The rows correspond to the different atmospheric layers and synoptic conditions to highlight the differences in organic/inorganic composition and multi-component internal mixing state of particles identified in this study.

1070

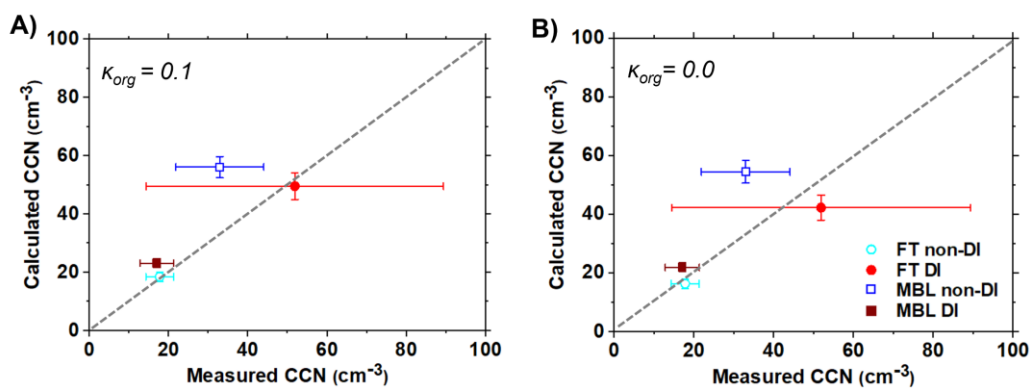


Figure 7. Comparison of the CCN concentration predicted from the particle size distribution and OVF with field measured CCN by onboard instruments across the different atmospheric layer and transport event. A) $\kappa_{org} = 0.1$; B) $\kappa_{org} = 0.0$. Grey dashed line corresponds to the 1:1 calculated CCN to measured CCN.

1075